

ELECTRON SPIN RESONANCE OF FLUX-GROWN STANNIC  
OXIDE SINGLE CRYSTALS

By

JERALD ARDEN TUNHEIM

Bachelor of Arts  
South Dakota State University  
Brookings, South Dakota  
1962

Master of Science  
South Dakota State University  
Brookings, South Dakota  
1964

Submitted to the Faculty of the Graduate College  
of the Oklahoma State University  
in partial fulfillment of the requirements  
for the degree of  
DOCTOR OF PHILOSOPHY  
May, 1968

1920  
1921  
1922

1923  
1924  
1925

1926

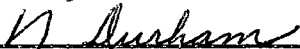
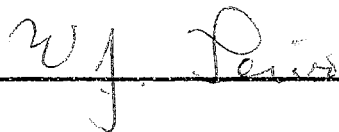
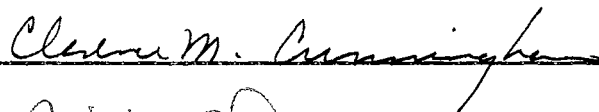
OCT 29 1968

ELECTRON SPIN RESONANCE OF FLUX-GROWN STANNIC  
OXIDE SINGLE CRYSTALS

Thesis Approved:



Thesis Adviser



Dean of the Graduate College

688836

## ACKNOWLEDGMENTS

The author wishes to express his deepest appreciation to many friends and associates whose assistance made this work possible. To Professor E. E. Kohnke, Thesis Chairman, go a special thanks for his guidance throughout the course of this investigation and the writing of this thesis. The author also wishes to extend a special thanks to Professor W. J. Leivo for his guidance during the course of this research. Gratitude is also expressed to Dr. M. D. Bell for his help and encouragement and to Paul Klingsporn whose assistance and cooperation made this work possible.

He is further indebted to fellow members of the research groups of Professor E. E. Kohnke and Professor W. J. Leivo for their suggestions and stimulating discussion, with special thanks to Gary Baum for his particularly valuable contributions.

He graciously acknowledges financial support of The National Aeronautics and Space Administration in the form of a Research Assistantship. And finally he wishes to express his gratitude to his wife, Patricia, for her encouragement and assistance throughout his graduate career.

## TABLE OF CONTENTS

Chapter	Page
I. INTRODUCTION . . . . .	1
Background Information. . . . .	1
Scope of the Present Study. . . . .	2
II. THEORETICAL BACKGROUND . . . . .	4
General Aspects . . . . .	4
The Spectroscopic Splitting Factor. . . . .	6
Hyperfine Coupling. . . . .	8
Observation of ESR and Kramers' Theorem . . . . .	10
Crystal Field Effects on Transition Metal Ions. . . . .	12
Spin Orbit Coupling . . . . .	20
Electric Dipole Selection Rules . . . . .	21
III. APPARATUS AND SAMPLES. . . . .	23
Apparatus . . . . .	23
Crystals Used . . . . .	25
Sample Crystal Structure. . . . .	26
IV. RESULTS AND CONCLUSIONS CONCERNING ION STUDIES . . . . .	32
Identification of the Nickel Center . . . . .	32
Orientation Dependence of the Nickel Spectrum . . . . .	35
Crystal Field Effects on Ni <sup>3+</sup> in SnO <sub>2</sub> . . . . .	40
Superhyperfine Structure of Ni <sup>3+</sup> . . . . .	46
ESR of Cr <sup>3+</sup> in Flux-grown SnO <sub>2</sub> . . . . .	51
ESR of Fe <sup>3+</sup> in SnO <sub>2</sub> . . . . .	58
ESR of unknown Interstitial Ion . . . . .	66
Numbers of Observed Centers . . . . .	69
V. RESULTS AND CONCLUSIONS CONCERNING HEAT TREATMENT EFFECTS. . . . .	71
Preliminary Remarks . . . . .	71
Visual Observations . . . . .	71
Heat Treatment Dependence of the ESR Spectrum . . . . .	73
Proposed Model. . . . .	75
VI. SUMMARY. . . . .	81
VII. SUGGESTIONS FOR FURTHER STUDY. . . . .	83

TABLE OF CONTENTS (Continued)

Chapter	Page
BIBLIOGRAPHY . . . . .	86
APPENDIX . . . . .	89

LIST OF TABLES

Table	Page
I. Degeneracies of States for Various Crystalline Symmetries . .	12
II. Character Table for the Point Group $D_{2h}$ . . . . .	18
III. Character Table for the $O_h$ Symmetry Group . . . . .	41
IV. Character Table for the $O_h$ Double Group . . . . .	43
V. Theoretical Intensity Ratios . . . . .	61
VI. Spin Concentration in Two Selected Samples . . . . .	70

LIST OF FIGURES

Figure	Page
1. Possible Splittings of a Two-Electron System in a Crystalline Environment . . . . .	11
2. Schematic Energy Level Diagram for $\text{Cu}^{2+}$ in $\text{SnO}_2$ . . . . .	20
3. Orientation Mount . . . . .	24
4. The Unit Cell of $\text{SnO}_2$ . . . . .	27
5. Unit Cell as Viewed Along the $[110]$ Direction . . . . .	28
6. Unit Cell as Viewed Along the $[\bar{1}\bar{1}0]$ Direction . . . . .	29
7. The Octahedrally Coordinated Interstitial Site in $\text{SnO}_2$ . . . . .	30
8. Comparison of the Signal due to $\text{Ni}^{3+}$ : (a) Before Diffusion (b) After First Diffusion, and (c) After Second Diffusion With the Corresponding $\text{Fe}^{3+}$ Signals (b), (d) and (e) . . . . .	34
9. Observed Resonances of $\text{Ni}^{3+}$ in the X-Y Plane. . . . .	36
10. Observed and Calculated Resonances of $\text{Ni}^{3+}$ in the X-Z and Y-Z Planes. . . . .	37
11. Observed and Calculated Resonances of $\text{Ni}^{3+}$ in the X-Y Plane . . . . .	38
12. Splitting of the $\text{Co}^{2+}$ Ground State in $\text{MgO}$ . . . . .	44
13. Splitting Factors for Trigonal Symmetry . . . . .	45
14. Resonance of $\text{Ni}^{3+}$ for $H_0$ Parallel to the X-axis . . . . .	47
15. Resonance of $\text{Ni}^{3+}$ for $H_0$ $10^\circ$ From the X-axis in the $\{001\}$ Plane . . . . .	48
16. Resonance of $\text{Ni}^{3+}$ for $H_0$ Parallel to the Y-axis . . . . .	49
17. Resonance of $\text{Ni}^{3+}$ for $H_0$ Parallel to the Z-axis . . . . .	50
18. Orientation Dependence in the $\{001\}$ Plane of Substitutional $\text{Cr}^{3+}$ ESR Signal. . . . .	52



LIST OF FIGURES (Continued)

Figure	Page
19. Orientation Dependence in the {110} Plane of Substitutional Cr <sup>3+</sup> ESR Signal . . . . .	53
20. Orientation Dependence of Interstitial Cr <sup>3+</sup> ESR Signal in the {001} Plane . . . . .	54
21. Orientation Dependence of Interstitial Cr <sup>3+</sup> ESR Signal in the {110} Plane . . . . .	55
22. ESR Signal of Substitutional Cr <sup>3+</sup> for H <sub>0</sub> Parallel to the Y-axis . . . . .	56
23. ESR Signal of Interstitial Cr <sup>3+</sup> for H <sub>0</sub> Parallel to the X-axis . . . . .	57
24. Orientation Dependence of Fe <sup>3+</sup> ESR Signal in the {001} Plane . . . . .	59
25. Orientation Dependence of Fe <sup>3+</sup> ESR Signal in the {110} Plane . . . . .	60
26. ESR Signal of $\pm\frac{1}{2}$ Transition of Fe <sup>3+</sup> for H <sub>0</sub> Parallel to the [110] Axis . . . . .	62
27. ESR Signal of $\pm\frac{1}{2}$ Transition of Fe <sup>3+</sup> for H <sub>0</sub> Parallel to the [001] Axis . . . . .	63
28. ESR Signal of the $\pm\frac{3}{2}$ Transition of Fe <sup>3+</sup> for H <sub>0</sub> Parallel to the [110] Axis . . . . .	64
29. ESR Signal of the $\pm\frac{3}{2}$ Transition of Fe <sup>3+</sup> for H <sub>0</sub> Parallel to the [001] Axis . . . . .	65
30. Resonance Due to Unknown Ions in the [001] Planes . . . . .	67
31. ESR Signal Due to Unknown Ion for H <sub>0</sub> Parallel to the [110] Axis . . . . .	68
32. Weight Gain for Oxygen Heat Treatment . . . . .	77
33. Weight Loss for Nitrogen Heat Treatment . . . . .	78
34. Ground State Energies . . . . .	79
35. Gaussian Curve . . . . .	88
36. Derivative Curve . . . . .	88

## CHAPTER I

### INTRODUCTION

#### Background Information

Although the electrical properties of stannic oxide ( $\text{SnO}_2$ ) have been studied and utilized in thin film and ceramic forms for some time, grown stannic oxide crystals<sup>1,2</sup> have been available only recently. Optical and electrical measurements on these samples<sup>3-7</sup> were in a general sense consistent with those previously taken on natural cassiterite samples.<sup>8,9</sup> That is, they exhibited broad-band semiconductor characteristics with larger electron mobilities and smaller effective masses than titanium dioxide ( $\text{TiO}_2$ ) specimens of the same crystal structure, together with a larger optical bandgap of  $\approx 4\text{eV}$  compared to  $\approx 3\text{eV}$  for  $\text{TiO}_2$ .

Quantitatively, however, limited correlation exists between the results of various groups working on  $\text{SnO}_2$  since the electrical conductivity at ordinary temperatures is a defect-controlled process for this material. Thus one expects variations arising from differences in both concentration and species of impurity ions introduced during the growth process and of other defects (surface or bulk) introduced thereafter.

In order to design meaningful experiments and correlate the results, one must have considerable knowledge concerning the type of defects present, their concentrations, and their interaction with the

surrounding crystal. Since electron spin resonance (ESR) can provide information about all three of these areas for the paramagnetic system, it seems appropriate that a comprehensive study of paramagnetic defects be made using this technique. This should contribute not only to knowledge of the defects themselves, but also aid in isolating intrinsic parameters of the crystal from those due to impurities present.

Since  $\text{SnO}_2$  has the same structure as the maser host<sup>9</sup>  $\text{TiO}_2$ , it seems very possible the ESR studies of transition metal and rare earth ions could pave the way for its utilization as a maser host. Furthermore, because of its larger forbidden gap,  $\text{SnO}_2$  unlike  $\text{TiO}_2$ , is still relatively transparent in the visible region after doping with transition metal impurities. This makes it a potential candidate as a laser host as well.

#### Scope of the Present Study

In this study, the four prominent ESR signals observed at room temperature in flux-grown  $\text{SnO}_2$  are identified as arising from the transition metal ions  $\text{Ni}^{3+}$ ,  $\text{Fe}^{3+}$ , and  $\text{Cr}^{3+}$ . Chromium ions are found to occupy both substitutional and interstitial sites, both giving rise to a rather large superhyperfine structure. Only limited discussion of these signals is made since they have been considered previously in the literature.<sup>10,11</sup>  $\text{Fe}^{3+}$  is found to occupy a substitutional position in the lattice and a superhyperfine structure is observed and discussed. Again only limited discussion of the spin Hamiltonian is made since it too has been reported previously.<sup>12</sup> The trivalent  $\text{Ni}^{3+}$  ion is found to occupy an interstitial position much like that of  $\text{Cr}^{3+}$ . Since it has not been reported previously, a more extensive analysis is given.

Changes in the ESR signals with heat treatment have been observed and a model is proposed to explain them. Microbalance data which supports the model is also presented. Finally, based on this model, a qualitative energy level scheme is proposed for the ground states of these ions relative to the conduction band of the host  $\text{SnO}_2$ .

## CHAPTER II

### THEORETICAL BACKGROUND

#### General Aspects

Many excellent discussions<sup>13-17</sup> of the general theory of ESR exist. The basic concept will be only briefly touched upon here while specific attention will be given to those details of theory involving group theoretical reasoning, which are directly pertinent to the work at hand and are not explicitly covered in the work of Pake<sup>13</sup> and Low<sup>15</sup>.

ESR may occur whenever a system of electrons has a net magnetic moment, and in general will involve a net contribution from both the spins and orbitals of several electrons. The cases investigated in this study are of this nature where  $\text{Cr}^{3+}$ , and  $\text{Ni}^{3+}$  each has three contributing electrons and  $\text{Fe}^{3+}$  has five. For the sake of simplicity, however, one can first consider the case of a paramagnetic center formed by a single electron as an illustration.

In the absence of a magnetic field the ground state is doubly degenerate in spin. This is assured by Kramers Theorem derived from the requirement of invariance of the system under time reversal (see page 10). However, when an external magnetic field  $H_0$  is applied to the system, the interaction  $\mu \cdot H_0$  removes this degeneracy. The term  $\mu$  in this expression is the effective magnetic moment of the electron reflecting both its spin and orbital motion. It can be expressed as

$\mu = g\beta S$  where  $g$  is a constant relating the effective magnetic moment to the spin  $S$  in terms of the Bohr magneton  $\beta$ . The separation of the levels is then given by

$$W = g\beta H_0 . \quad (1)$$

If an alternating magnetic field is applied perpendicular to  $H_0$  at a frequency  $\nu$  such that,

$$h\nu = g\beta H_0 , \quad (2)$$

where  $h$  is Planck's constant, magnetic dipole transitions will occur between the two levels. These transitions, corresponding in a classical sense to flipping the electron spin, cause an absorption of energy from the oscillating field for a transition upward and a loss of the same amount of energy to the field for a transition downward. Since both transitions have the same a priori probability, a net absorption of energy is only realized if the lower state has a larger population.

This condition is met if the system is in thermal equilibrium, since the distribution of spins is given by the Boltzman expression

$$\frac{N_+}{N_-} = \exp \left( \frac{-W}{kT} \right) \quad (3)$$

where  $N_+$  and  $N_-$  are the numbers of electrons in the upper and lower levels, respectively;  $k$  is the Boltzman constant and  $T$  is the absolute temperature of the system. Thus the relaxation time of the electron from the higher to the lower level is very important to the observation of the electron resonance. For example, if the relaxation time is long, the microwave field may induce transitions upward faster than the spontaneous emission downward until the populations become almost equal at which time very little net energy is absorbed by the system. This condition in ESR is called "saturation".

Two major relaxation processes occur in a paramagnetic system. The first is due to magnetic dipole interaction between the paramagnetic centers called spin-spin relaxation, which causes thermal equilibrium within the spin system. The second is due to interaction between the paramagnetic center and its diamagnetic neighbors, causing thermal equilibrium between the spin and lattice systems. This second relaxation process, called spin-lattice relaxation, is obviously of primary interest here, since it allows the transfer of energy out of the spin system resulting in a net absorption of the microwave energy. Also, it is the process dependent on the crystal field of the host and therefore relinquishes information about the crystal field parameters. A strong coupling to the lattice results in a short relaxation time while weaker couplings give longer relaxation times. The power at which saturation occurs is thus an important measured quantity.

#### The Spectroscopic Splitting Factor

For the free ion case the value of  $g$  in Equation 1 is the Lande  $g$ -factor which under of assumption of L-S coupling is given by

$$g = 1 + \frac{J(J+1) + S(S+1) - L(L+1)}{2J(J+1)} \quad (4)$$

However, by considering a few examples one can see that the experimental  $g$ -values for the case of an ion in a crystal is not the free ion Lande  $g$ -factor. The  $g$ -value from Equation 1 is then called the spectroscopic splitting factor and used as a parameter to describe the experimental data. It contains a combination of orbital and spin contributions which act together to cause an effective magnetic moment. Since the orbital factors are very dependent on the crystal field, this  $g$ -value depends

on the orientation of the external magnetic field with respect to the crystal field. Therefore the spectroscopic splitting factor instead of being a scalar quantity is indeed a tensor of second rank and should be written in general as the 3X3 matrix

$$\underline{g} = \begin{pmatrix} g_{xx} & g_{xy} & g_{xz} \\ g_{yx} & g_{yy} & g_{yz} \\ g_{zx} & g_{zy} & g_{zz} \end{pmatrix} \quad (5)$$

One can, however, transform to a principal axis system and diagonalize this tensor, allowing it to be written in dyadic notation as

$$\underline{g} = \vec{i} g_x \vec{i} + \vec{j} g_y \vec{j} + \vec{k} g_z \vec{k} \quad (6)$$

where  $g_x = g_{xx}$ ,  $g_y = g_{yy}$  and  $g_z = g_{zz}$ . One should note here that these principal axes are "magnetic axes" and do not in general coincide with the crystalline axes. The magnetic field with respect to the axis system can then be written

$$\vec{H}_0 = H_x \vec{i} + H_y \vec{j} + H_z \vec{k} \quad (7)$$

One can now write an effective spin Hamiltonian in the form

$$H = \beta \vec{H}_0 \cdot \underline{g} \cdot \vec{S} \quad (8)$$

In this equation it is seen that the quantity  $\vec{H}_0 \cdot \underline{g}$  is a vector which can in general vary in both direction and magnitude from the applied field  $\vec{H}_0$ . It can be thought of as an "effective magnetic field" which is a combination of the applied magnetic field and that of the electron orbitals. Combining Equations 6 and 7 in the conventional dot product gives

$$\vec{H}_0 \cdot \underline{g} = g_x H_x \vec{i} + g_y H_y \vec{j} + g_z H_z \vec{k} \quad (9)$$



However, using spherical polar coordinates leads to the relations

$$\begin{aligned} H_x &= H_0 \sin\theta \cos\phi \\ H_y &= H_0 \sin\theta \sin\phi \\ H_z &= H_0 \cos\theta \end{aligned} \quad (10)$$

where  $\theta$  and  $\phi$  are the conventional angles of spherical polar coordinates and  $H_0 = |\vec{H}_0|$ . Equation 9 can then be written as

$$\vec{H}_0 \cdot \underline{g} = H_0 (g_x \sin\theta \cos\phi \vec{i} + g_y \sin\theta \sin\phi \vec{j} + g_z \cos\theta \vec{k}). \quad (11)$$

Taking the axis of quantization as the direction of the "effective magnetic field", one can use the magnitude of the effective field and reduce Equation 8 to the scalar equation

$$H = \beta \sqrt{g_x^2 \sin^2\theta \cos^2\phi + g_y^2 \sin^2\theta \sin^2\phi + g_z^2 \cos^2\theta} H_0 S. \quad (12)$$

Using this form for the Hamiltonian and the spin eigenvalue  $\pm \frac{1}{2}$ , the energy separation of the spin states can be written as,

$$W = g\beta H_0$$

where now

$$g = \sqrt{g_x^2 \sin^2\theta \cos^2\phi + g_y^2 \sin^2\theta \sin^2\phi + g_z^2 \cos^2\theta}. \quad (13)$$

### Hyperfine Coupling

A coupling which has not yet been considered is that of the nearby nuclei with the unpaired electron, i.e., the hyperfine coupling. There are basically two interactions involved.<sup>13</sup> The first is an ordinary dipole-dipole coupling between the electron and a nuclear magnetic moment given by

$$- g_N g \beta \beta_N \langle r^{-3} \rangle [ \vec{I} \cdot \vec{S} - 3(\vec{I} \cdot \vec{r})(\vec{S} \cdot \vec{r}) ], \quad (14)$$

where  $g_N$  is the nuclear  $g$  value,  $\beta_N$  is the nuclear magneton,  $I$  is the spin quantum number of the particular nucleus involved and  $\vec{r}$  is the radius vector between the electron and that nucleus. The second is the Fermi contact energy which arises when the electron wave function is non-zero at the particular nucleus. It can be written in the form,

$$\frac{8\pi}{3} g g_N \beta \beta_N \delta(\vec{r}) \vec{I} \cdot \vec{S} \quad (15)$$

where  $\delta(\vec{r})$  is that Dirac delta function making the function zero everywhere except at the nucleus.

Since the knowledge of the true electron wave function is generally insufficient to calculate expectation values of these terms, both are included in the linear combination of terms involving  $S$  and  $I$ :

$$\sum_{\alpha, \alpha' = x, y, z} A_{\alpha\alpha'} S_{\alpha} I_{\alpha'} \quad (16)$$

where  $A_{\alpha\alpha'}$  is a component of an unknown second rank tensor. However, one can always transform this tensor to a set of principal axes giving only the diagonal terms

$$A_x I_x S_x + A_y I_y S_y + A_z I_z S_z \quad (17)$$

or

$$\vec{I} \cdot \underline{A} \cdot \vec{S}. \quad (18)$$

It should be noted here that it is not necessary for the principal axes of this hyperfine tensor and the  $g$ -tensor to coincide. If they don't, then cross terms must be considered when calculating energy levels.

Combining Equations 8 and 17, one has a more general Hamiltonian

$$H = \beta \vec{H} \cdot \underline{g} \cdot \vec{S} + \vec{I} \cdot \underline{A} \cdot \vec{S}. \quad (19)$$

The last term to be discussed is the so-called "zero-field splitting" which arises in a spin system of  $S > \frac{1}{2}$ . It is an interaction between unpaired electrons which may for example break a four-fold spin degenerate ground state into two doublets. This term can be written in the form

$$\vec{S} \cdot \underline{D} \cdot \vec{S} \quad (20)$$

where  $\underline{D}$  is a second rank tensor. The splitting caused by this term is on the order of  $0.1 \text{ cm}^{-1}$ . A completely general Hamiltonian in usable form including this term cannot be derived since both the electron orbital and the particular crystal symmetry are involved. However, for a rhombic system the form of the effective spin Hamiltonian including the discussed terms has been given by Low<sup>14</sup> as

$$\begin{aligned} H_{\text{rhombic}} = & \beta(g_z H_z S_z + g_x H_x S_x + g_y H_y S_y) \\ & + D[S_z^2 - \frac{1}{3}(S)(S+1)] + E(S_x^2 - S_y^2) \\ & + A_z S_z I_z + A_x S_x I_x + A_y S_y I_y. \end{aligned} \quad (21)$$

It is seen in this case that the zero-field splitting can be represented by the two constants D and E.

#### Observation of ESR and Kramers' Theorem

Although a net magnetic moment and an appropriately short relaxation time are necessary requirements for observation of an ESR absorption, they are not sufficient. There is also the requirement that the crystal field splittings must not leave the ground state a singlet with other spin states separated from it by more than the microwave photon energy ( $\sim 0.3 \text{ cm}^{-1}$  for X-band spectrometers). For example, a system of two electrons with  $S = 1$  might be split in the manner shown in Figure 1:

$$\begin{array}{l} \text{----- } S_z = +1 \\ \text{----- } S_z = 0 \end{array}$$

Figure 1. Possible Splitting of  
Two-Electron System  
in a Crystalline  
Environment

If the crystal field splitting is very large compared to the microwave energy ( $h\nu$ ), no transitions from the ground state to higher states will take place. Moreover, the transition between the  $S_z = \pm 1$  levels is forbidden although the crystal field may partially break this forbiddenness. The population of these latter levels will generally be small, particularly for very low temperatures. Observation of a signal for this type of system would be unlikely.

For systems of an odd number of electrons, one is assured that the ground state is degenerate by the well-known Kramers theorem. This theorem states that for any system composed of an odd number of electrons the ground state is at least two-fold degenerate in the presence of any crystal field. This condition, shown by Wigner<sup>18</sup> to be due to invariance of the system under time reversal, has been discussed quite simply by Low.<sup>14</sup> Although a formal discussion is more involved, the condition basically evolves from the requirement that  $\vec{L} \cdot \vec{S} = (\vec{r} \times \vec{p}) \cdot \vec{S}$  be invariant under time reversal. When  $t \rightarrow -t$ ,  $\vec{p} \rightarrow -\vec{p}$ ; since  $\vec{r}$  is invariant, one must let  $\vec{S} \rightarrow -\vec{S}$ . From this one can show that two linearly independent eigenfunctions of the same energy must exist for  $\pm S$ . Thus, as an example,  $S = \frac{3}{2}$  gives for even lowest symmetry the three doubly degenerate levels  $S_z = \pm \frac{5}{2}$ ,  $\pm \frac{3}{2}$ , and  $\pm \frac{1}{2}$ . One might notice here, however, that the only allowed transition satisfying the

requirement  $\Delta S_z = \pm 1$  is the last of the three. This level many times forms the ground state of the system and gives rise to the most prominent of the observed signals, although for lower symmetries the other two are also partially allowed because of the crystal field perturbation. The effect of Kramers' theorem can be seen in the Table I, since no half-integer J results in a degeneracy less than two.

TABLE I  
DEGENERACIES OF STATES FOR VARIOUS CRYSTALLINE SYMMETRIES  
(After Low<sup>14</sup>)

System	Degen- eracy	J						Degen- eracy	$\frac{1}{2}$	$\frac{3}{2}$	$\frac{5}{2}$	$\frac{7}{2}$	$\frac{9}{2}$	$\frac{11}{2}$	
		0	1	2	3	4	5								
Cubic ( $O_h, T_d$ )	1	1	0	0	1	1	0	2	1	3	1	2	1	2	
	2	0	0	1	0	1	1	4	0	1	1	1	2	2	
	3	0	1	1	2	2	3								
Tetragonal ( $D_{2h}, D_{4h}, D_4, D_{4h}$ )	1	1	1	3	3	5	5	2	}	1	2	3	4	5	6
	2	0	1	1	2	2	3								
Hexagonal ( $D_{3h}, D_6, D_{6h}$ )	1	1	1	1	3	3	3								
	2	0	1	2	2	3	4								
Trigonal ( $C_{3v}, D_{3d}, D_3$ )	1	1	1	1	3	3	3								
	2	0	1	2	2	3	4								
Rhombic ( $C_{2v}, D_2, D_{2h}$ )	1	1	3	5	7	9	11								
Triclinic ( $C_1, C_i$ )															
Monoclinic ( $C_3, C_2, C_{2h}$ )															
and all others															

### Crystal Field Effects on Transition Metal Ions

When a transition metal ion occupies some position in a solid, the effects of the crystal field on it are profound. Ideally one would like to solve the Schrodinger equation for the complete crystal system, or

at least for a limited number of atoms in the vicinity of the ion. Obviously the first approach is a practical impossibility; however, the second under certain approximations has been attempted with limited success.<sup>19,20</sup>

The most widely used calculations are those based on a so-called "crystal field theory". This theory assumes that the effect of the host crystal on an ion can be described in terms of the field due to a symmetric array of point charges. Although the approximations of these calculations are undoubtedly gross, their value cannot be denied since they allow a relatively easy solution of the problem and results can be correlated at least qualitatively with experimental data. For a more complete exposition of the general theory the reader is referred to references 21-25, and the particularly good discussion of this problem for the experimentalist given by Low.<sup>14</sup> The emphasis present here will be placed only on general concepts and on an extension of a simple method of Bethe<sup>26</sup>. This approach is very valuable when employed in a treatment for low symmetry systems which makes use of information already known for more symmetrical systems.

As mentioned above, in the crystal field approximation of the surrounding ions are assumed to act as point charges which set up a static electric field acting on the ion of interest. Knowing the symmetry of the site, the experimentalist can use the effective charge of the ions as an adjustable parameter. The Hamiltonian in this approximation can be written as

$$H = \sum_{K=1}^N \frac{p^2}{2m} + V_F + V_{LS} + V_{SS} + V_N + V_Q + V_C, \quad (22)$$

with the following origins for the various terms:

$$\sum_{K=1}^N \frac{p^2}{2m}, \text{ the kinetic energy of the electron system}$$

$V_F$ , the coulomb electron-nuclear and electron-electron interaction

$V_{LS}$ , the spin-orbit coupling

$V_{SS}$ , the spin-spin coupling

$V_N$ , the hyperfine coupling of the nucleus to the electron system

$V_Q$ , the electrostatic interaction with the quadrupole moment  $Q$  of the nucleus

$V_C$ , the potential due to the crystal surroundings.

In order to be able to use perturbation theory, one must know the relative magnitudes of the above terms. These can be estimated for first five potential terms from free ion spectroscopic data, e.g., for the first transition series (the iron group)

$$V_F \sim 10^5 \text{ cm}^{-1}$$

$$V_{LS} \sim 10^2 \text{ cm}^{-1}$$

$$V_{SS} \sim 1 \text{ cm}^{-1}$$

$$V_N \sim 10^{-1} \text{ cm}^{-1} - 10^{-3} \text{ cm}^{-1}$$

$$V_Q \sim 10^{-3} \text{ cm}^{-1}.$$

In the perturbation treatment of this problem three cases exist depending on the value of  $V_C$ . The strong field case exists when  $V_C$  is of the same order of magnitude as  $V_F$ . This case occurs when a strong covalent interaction is present, making results based upon an electrostatic interaction approximation (i.e., on "crystal field theory") relatively meaningless. The medium field case exists for many of the iron group ions in crystals. This arises when  $V_C$  is smaller than  $V_F$  but larger than  $V_{LS}$ . For this case the perturbation due to  $V_C$  can be

calculated before  $V_{LS}$  is applied. The third case is the weak field case when  $V_C$  is less than  $V_{LS}$ . This is more applicable to the situation for rare earths in crystals, since  $V_{LS}$  is about an order of magnitude larger for these ions than for those of the iron group.

Since a crystal field potential (treated as an electrostatic potential), obeys Laplace's equation, it may be expressed in terms of the generalized Legendre polynomials as<sup>21</sup>

$$V = \sum_n \sum_{m=-n}^n \sum_k A_n^m r^n Y_n^m(\theta_k, \phi_k) = \sum_n \sum_m V_n^m \quad (23)$$

where  $k$  expresses a summation over the electrons of the system and  $Y_n^m(\theta_k, \phi_k)$  are the normalized spherical harmonics. This form is particularly inviting since the orbitals to be employed are usually in the form of spherical harmonics, which of course form a basis for the irreducible representations of the complete rotation group. A matrix element of the form  $\langle JM | V_n | J'M' \rangle$  thus can be represented in terms of the well-known Wigner coefficients.<sup>24,27</sup> This allows the calculation of the relative splitting of several levels in terms of some parameter. By convention this quantity is usually called  $Dq$  and involves the effective charge of the transition metal ion, the bond distance from it to the surrounding ions, and the effective charge of the surrounding ions.<sup>22</sup>

This form of the matrix element allows one to limit the number of potential terms which must be considered. The matrix elements of the form  $\psi_J^M V_n^m \psi_J^{M'}$  are zero if  $V_n^m$  is of order  $>2J$ . This is obvious from the requirement that the direct product of the irreducible representations of  $\psi_J^M$ ,  $V_n^m$ , and  $\psi_J^{M'}$  contain the completely symmetric representation



$D^{(0)}$ . In order for this condition to be met, the direct product of  $\psi_J^M$  and  $\psi_J^{M'}$  must contain the irreducible representation of  $V_n^m$ , which it cannot if  $V_n^m$  is of greater order than  $2J$ . Thus for D-states the highest order which must be considered is  $n = 4$  and for F-states,  $n = 6$ . Also any odd values of  $V_n^m$  are eliminated since the product of  $\psi_J^M \psi_J^{M'}$  is always invariant under inversion and if  $V_n^m$  is not, the matrix element will be zero.

It should be mentioned here that calculation of matrix elements can also be made quite easily by using an alternative operator equivalent method developed by Stevens,<sup>28</sup> Elliott<sup>29</sup> and Judd.<sup>30</sup> A good discussion of this method together with the required tables is given by Low.<sup>14</sup>

Although calculations of the type discussed above are necessary in many cases, a simple qualitative group theoretical method of Bethe<sup>26</sup> together with experimental and theoretical data found in the literature often suffices for the experimentalist attempting to interpret initial ESR or optical absorption results. In general, this method utilizes the fact that the customary orbital functions are represented by the spherical harmonics which form a basis for the irreducible representations of the complete rotation group. Now if a perturbation  $H_1$  of lower than spherical symmetry is applied to the system, the total Hamiltonian  $H$  can be written as

$$H = H_0 + H_1 \quad (24)$$

where  $H_0$  is the Hamiltonian of the free ion. The eigenfunctions of this Hamiltonian must now form a basis for the irreducible representations of the symmetry group of  $H_1$ . In other words, the irreducible

representations of the complete rotation group are generally now reducible representations for the subgroup of  $H_1$ . Thus, the qualitative energy level splittings can be found using the well-known group theoretical expression for the number of times  $a_i$ , an irreducible representation, appears in a reducible representation given in reference 24,

$$a_i = \frac{1}{h} \sum_R X_i(R) X_r(R) \quad (25)$$

page 30, where  $h$  is the order of the group, the summation is over the elements  $R$  of the group,  $X_i(R)$  is the character of the irreducible representation  $i$  for symmetry element  $R$ , and  $X_r(R)$  is the character of the reducible representation for symmetry element  $R$ . Character tables for all of the common point groups have been calculated and are listed by several authors.<sup>24,31,32</sup>

As an example of this technique, consider the six oxygen ions surrounding a  $\text{Cu}^{2+}$  ion in a substitutional position of  $\text{SnO}_2$ . The ions in this case reduce the symmetry of the total Hamiltonian to  $D_{2h}$  which has the character table given on the following page. The characters of the  $D^{(2)}$  representation of the complete rotation group (the characters of the representation for which the d-orbitals of  $\text{Cu}^{2+}$  are a basis) are found by standard formulas<sup>(21, pp. 325-367)</sup> or by carrying out the  $D_{2h}$  symmetry operations on the d-orbitals and noticing how many are left invariant.

Using equation 25 one obtains

$$D^{(2)} = 2 A_{1g} + B_{1g} + B_{2g} + B_{3g}. \quad (26)$$

Thus the five-fold degeneracy of the d-orbitals is broken by the surrounding crystalline field into five singly degenerate states. To find

the representations to which each of the orbitals belong, one simply notices how they transform under the operations of the group  $D_{2h}$ , which gives,

$$\begin{aligned} 3Z^2 - r^2 & - - - A_{1g} \\ X^2 - Y^2 & - - - A_{1g} \\ xy & - - - B_{1g} \\ xz & - - - B_{2g} \\ zy & - - - B_{3g} \end{aligned}$$

TABLE II  
CHARACTER TABLE FOR THE POINT GROUP  $D_{2h}$

	E	$C_2^{(z)}$	$C_2^{(y)}$	$C_2^{(x)}$	I	$\sigma(xy)$	$\sigma(xz)$	$\sigma(yz)$
$A_{1g}$	1	1	1	1	1	1	1	1
$A_{1u}$	1	1	1	1	-1	-1	-1	-1
$B_{1g}$	1	1	-1	-1	1	1	-1	-1
$B_{1u}$	1	1	-1	-1	-1	-1	1	1
$B_{2g}$	1	-1	1	-1	1	-1	1	-1
$B_{2u}$	1	-1	1	-1	-1	1	-1	1
$B_{3g}$	1	-1	-1	1	1	-1	-1	1
$B_{3u}$	1	-1	-1	1	-1	1	-1	-1
$D^{(2)}$	5	1	1	1	5	1	1	1

where designation of orbitals on the left are the conventional d-orbitals used extensively in the literature.

Although this has given the final number of energy levels and their degeneracies, it has given no knowledge of the relative separations of the levels. This information can qualitatively be obtained by considering successive perturbations using the same technique as above. For example consider the previous calculations in terms of the series of perturbations  $R^3 \rightarrow O_h \rightarrow D_{4h} \rightarrow D_{2h}$  rather than the single perturbation  $R^3 \rightarrow D_{2h}$ . Obviously the largest perturbation is the first one. This would be the case where all of the  $O^{2-}$  ions were equal distances (cubic symmetry) from the  $Cu^{2+}$  ion and from each other. Using the  $D^{(2)}$  representation which was discussed previously, together with the  $O_h$  character table, one finds

$$D^{(2)} = E_g + T_{2g} . \quad (27)$$

Thus in first approximation the d-orbitals are split into a doublet and a triplet. From what is observed in similar systems this splitting is expected to be of the order of  $10^4 \text{ cm}^{-1}$ . For the next perturbation, use the character of  $E_g$  and  $T_{2g}$  and the character table  $D_{4h}$  (tetragonal symmetry) which gives

$$\begin{aligned} T_{2g} &= B_{2g} + E_g \\ E_g &= B_{1g} + A_{1g} . \end{aligned} \quad (28)$$

Thus the second perturbation breaks the system into three singly degenerate levels and one doubly degenerate level. This perturbation should be about an order of magnitude less than the previous one. Finally, using the characters of  $D_{4h}$  representations and the  $D_{2h}$  character table, one obtains the qualitative energy level diagram of Figure 2.

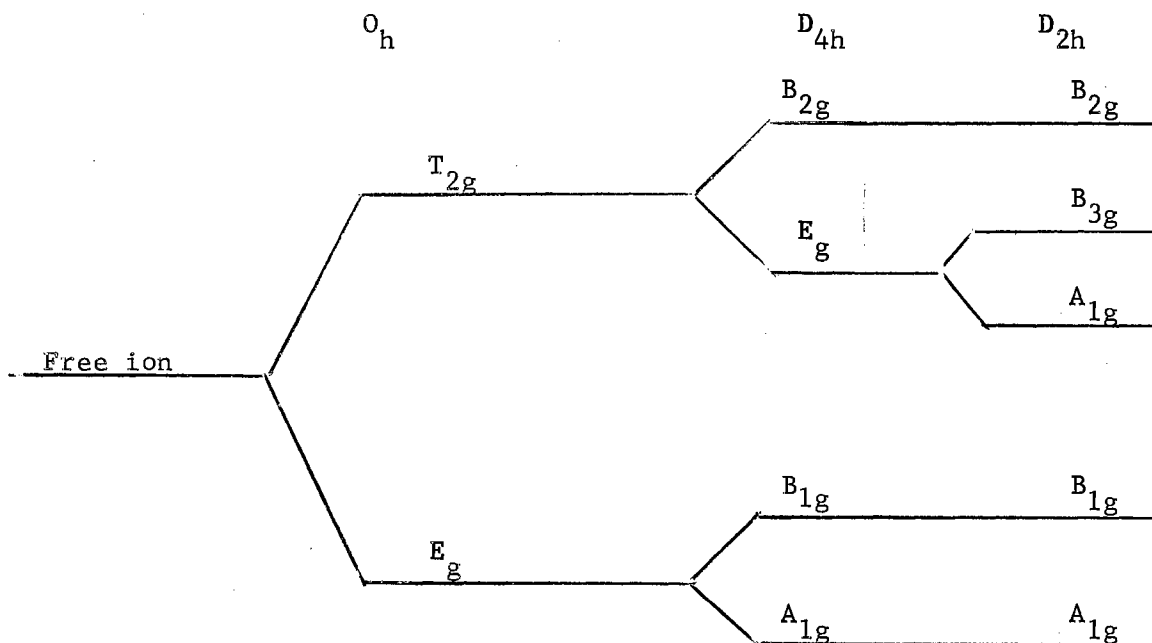


Figure 2. Schematic Energy Level Diagram for  $\text{Cu}^{2+}$  in  $\text{SnO}_2$

### Spin Orbit Coupling

In the above one notices that the discussion has avoided the perturbation due to spin-orbit coupling which of course must be included in the calculation. Since this is on the order of  $10^2 \text{ cm}^{-1}$  for the iron group, it can usually be considered last. However, one must look carefully at each specific case to insure that it has truly been included at the proper place in the order of the perturbations treated. The group theoretical reasoning is still the same except that the representation of the total wavefunction is the direct product of the irreducible representations of the spin and orbital parts. It then can be broken down into irreducible representations of the total symmetry group. For example,  $V^{3+}$  of  $S = 1$ , has a spin eigenfunction belonging to  $D^{(1)}$  of the complete rotation group. The reducible representation of the total wavefunction  $\Gamma_t$  is then given by

$$D^{(1)} \times \Gamma_o = \Gamma_t \quad (29)$$

where  $\Gamma_o$  is the irreducible representation of the orbital wavefunction. The characters of  $\Gamma_t$  can easily be found from the relation<sup>24</sup>

$$X_1(R) X_o(R) = X_t(R) \quad (30)$$

where  $X_1(R)$  is the character of  $D^{(1)}$ ,  $X_o(R)$  is the character of  $\Gamma_o(R)$ , and  $X_t(R)$  is the character of  $\Gamma_t$ , all for the symmetry element  $R$ . The representation  $\Gamma_t$  can then be broken down into irreducible representations of the total symmetry group by use of equation 25 giving the splittings due to spin-orbit coupling.

#### Electric Dipole Selection Rules

The electric dipole selection rules may now be found quite easily using the same type of arguments.<sup>21</sup> The matrix element  $H_{fi}$  in the golden rule formula<sup>33</sup> is of the form

$$H_{fi} = \int \psi_f A \psi_i d\tau \quad (31)$$

where  $\psi_f$  and  $\psi_i$  are the final and initial states of the system, respectively, and  $A$  is the electric dipole operator connecting the two states. This matrix element can be shown to be zero unless the direct product  $\Gamma_f \times \Gamma_A \times \Gamma_i$ , the representation of the matrix element, contains the completely symmetric representation. Here  $\Gamma_f$ ,  $\Gamma_A$ , and  $\Gamma_i$  are the representations of the final state, the electric dipole operator, and the initial state, respectively. Since the electric dipole operator behaves as a vector,<sup>24</sup> it belongs to the  $D^{(1)}$  representation of the complete rotation group. The characters for the reducible representation can then be found by the relation similar to equation 30,

$$\chi_H = \chi_f \chi_A \chi_i \quad (32)$$

where  $\chi_H$ ,  $\chi_f$ ,  $\chi_A$  and  $\chi_i$  are the characters of the representations of the total matrix element, the final state, the electric dipole operator, and the initial state, respectively. Whether the transition is allowed or forbidden then is determined by

$$a_1 = \frac{1}{h} \sum_R \chi_{A_1} \chi_H \quad (33)$$

where  $A_1$  is the number of times the completely symmetric representation appears in  $\Gamma_H$  and  $\chi_{A_1}$  is the character of the completely symmetric representation (value of 1 for all symmetry elements). If  $a_1 > 0$ , the transition is allowed if  $a_1 = 0$ , the transition is forbidden.

## CHAPTER III

### APPARATUS AND SAMPLES

#### Apparatus

Since the X-band ESR spectrometer employed in this study has been extensively described previously,<sup>34,35</sup> only the special equipment will be mentioned here.

In order that the Varian V-4531 ESR cavity with its associated variable temperature apparatus could be used to obtain orientation data, the orientation mount shown in Figure 32 was constructed. It fits directly onto the V-4531 cavity, allowing the sample to be rotated while at temperatures ranging from  $-180^{\circ}\text{C}$  to approximately  $+300^{\circ}\text{C}$  with an accuracy of  $\pm 0.1$  degree.

The crystals were oriented by the use of the Laue back-reflection technique and transfer apparatus described previously.<sup>35</sup> After mounting, the orientation of the samples could be checked to an accuracy of  $\pm 0.5^{\circ}$  by the particular symmetry of the observed ESR signals. The  $\text{Fe}^{3+}$  ion was particularly helpful in this respect since both the  $\{110\}$  and  $\{001\}$  planes can be checked by its use.

The nuclear magnetic resonance probe used to measure the magnetic field was that described by Bell.<sup>34</sup> It was found that the frequency could be lowered to allow low magnetic field measurements by simply increasing the length of the coaxial cable connecting the oscillator to



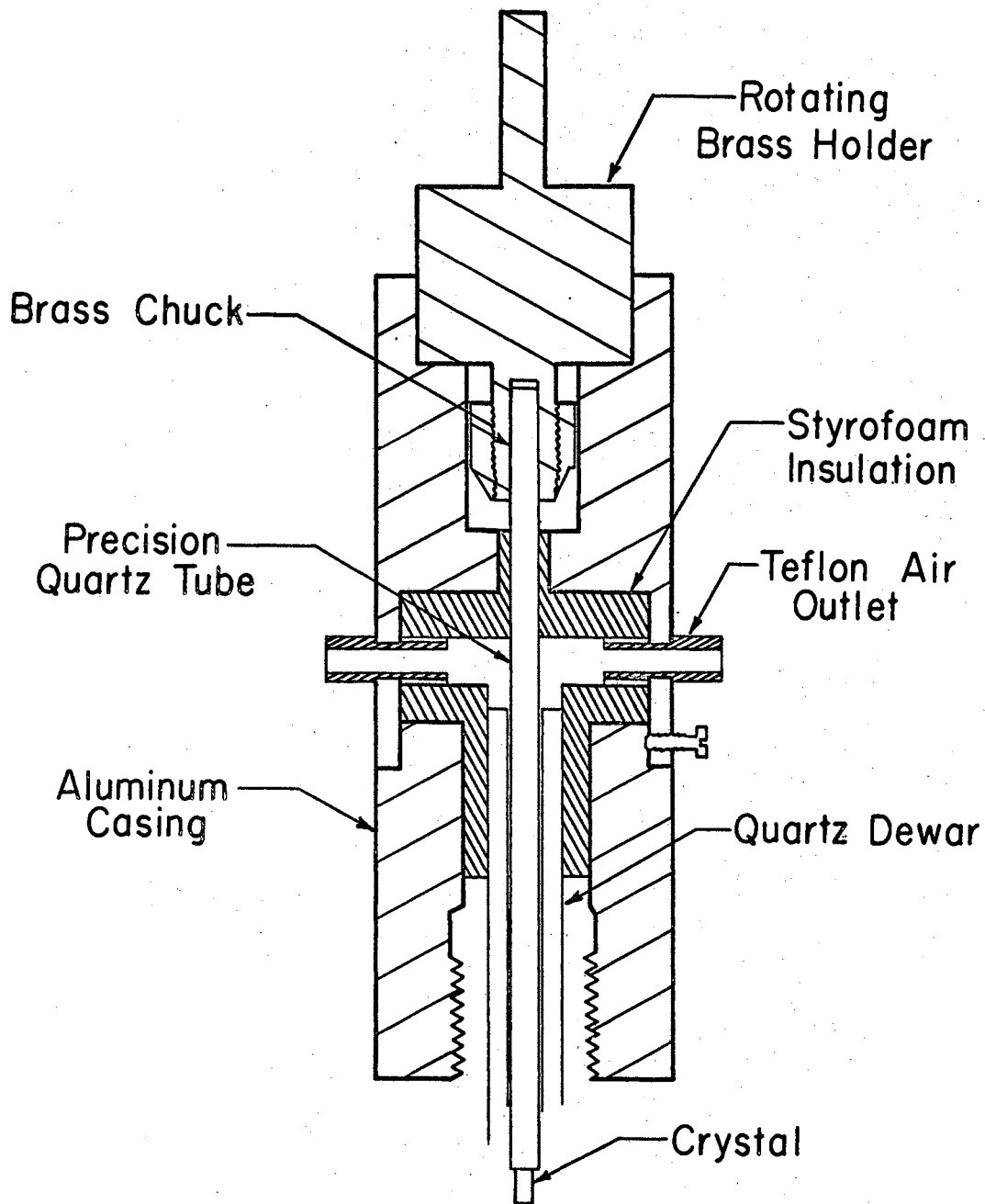


Figure 3. Orientation Mount

the probe by about 8 feet. Difficulty is encountered, however, for magnetic fields less than one thousand gauss. This could be possibly corrected by building an oscillator with larger power output or a new detection circuit.

#### Crystals Used

Crystals used in this study were grown by Kunkle<sup>1</sup> in a  $\text{CuO}_2$  flux. In this procedure two parts  $\text{Cu}_2\text{O}$  to one part  $\text{SnO}_2$  were placed in a platinum crucible and the mixture heated to temperatures ranging from  $1175^\circ\text{C}$  to  $1300^\circ\text{C}$ . Using this growth process Kunkle has grown a large number of crystals which are parallelepiped in shape, ranging in size from 3 mm x 1 mm x 1 mm to 1 mm x 0.5 mm x 0.5 mm. The growth axis is the c-axis and thus the end faces of the crystal are {001} planes while the other faces are {110} planes.

Spectrographic analysis (1) gave an impurity concentration of 0.002% by weight of  $\text{CuO}$  and 0.02%  $\text{SiO}_2$ . Since the concentration of paramagnetic impurities investigated in this work is much less than either of these (See Table VI), it is logical that they did not appear in the analysis.

Furthermore since the silicon impurity would probably be in a +4 state, it would not appear in the ESR spectra. Copper, however, should be in the paramagnetic +2 valence state and should thus give rise to an ESR resonance. It is felt at this time that this signal may only be observable at liquid helium temperatures for low power levels.

---

<sup>1</sup>Analysis by the Bruce Williams Laboratory, Joplin, Missouri.

## Crystal Structure

The symmetry of the  $\text{SnO}_2$  crystal is equivalent to that of the more well known rutile ( $\text{TiO}_2$ ). The space group is  $D_{4h}^{14}$  with a local symmetry of  $D_{2h}$  at the tin site. The lattice parameters of the unit cell as shown in Figure 4 are  $a = 4.737\text{\AA}$ ,  $c = 3.186\text{\AA}$  and  $u = 0.307$  with  $c/a = 0.672$ .

The substitutional position consists of two magnetically nonequivalent sites which can be transformed into one another by a  $90^\circ$  rotation. As a consequence the two sites are magnetically equivalent along the  $[100]$  and  $[010]$  directions. The distances between the surrounding ions and the undistorted lattice (after Kikuchi<sup>37</sup>) are given in Figures 5 and 6.

Two types of interstitial sites exist in the  $\text{SnO}_2$  host. The first shown in Figure 7 has the larger volume and thus seems to be the more likely place for an impurity ion to locate. It is surrounded by a distorted octahedron of oxygens with tetragonal symmetry with its tetragonal axis lying  $+13^\circ$  from the  $[110]$  axis. The total symmetry, however, is lowered to  $C_{2h}$  by another distorted octahedron of tin atoms of the same symmetry but with its tetragonal axis tilted  $-45^\circ$  from the  $[110]$  axis. Four inequivalent sites of this type exist<sup>11</sup> collapsing to two in the  $[110]$  and  $[100]$  directions. A typical ESR curve for an ion in this site will thus have the characteristics of Figure 9. The second possible interstitial site is surrounded by a distorted tetrahedron of oxygen ions. There are only two nonequivalent sites of this type per unit cell and they become magnetically equivalent in the  $[110]$  direction.

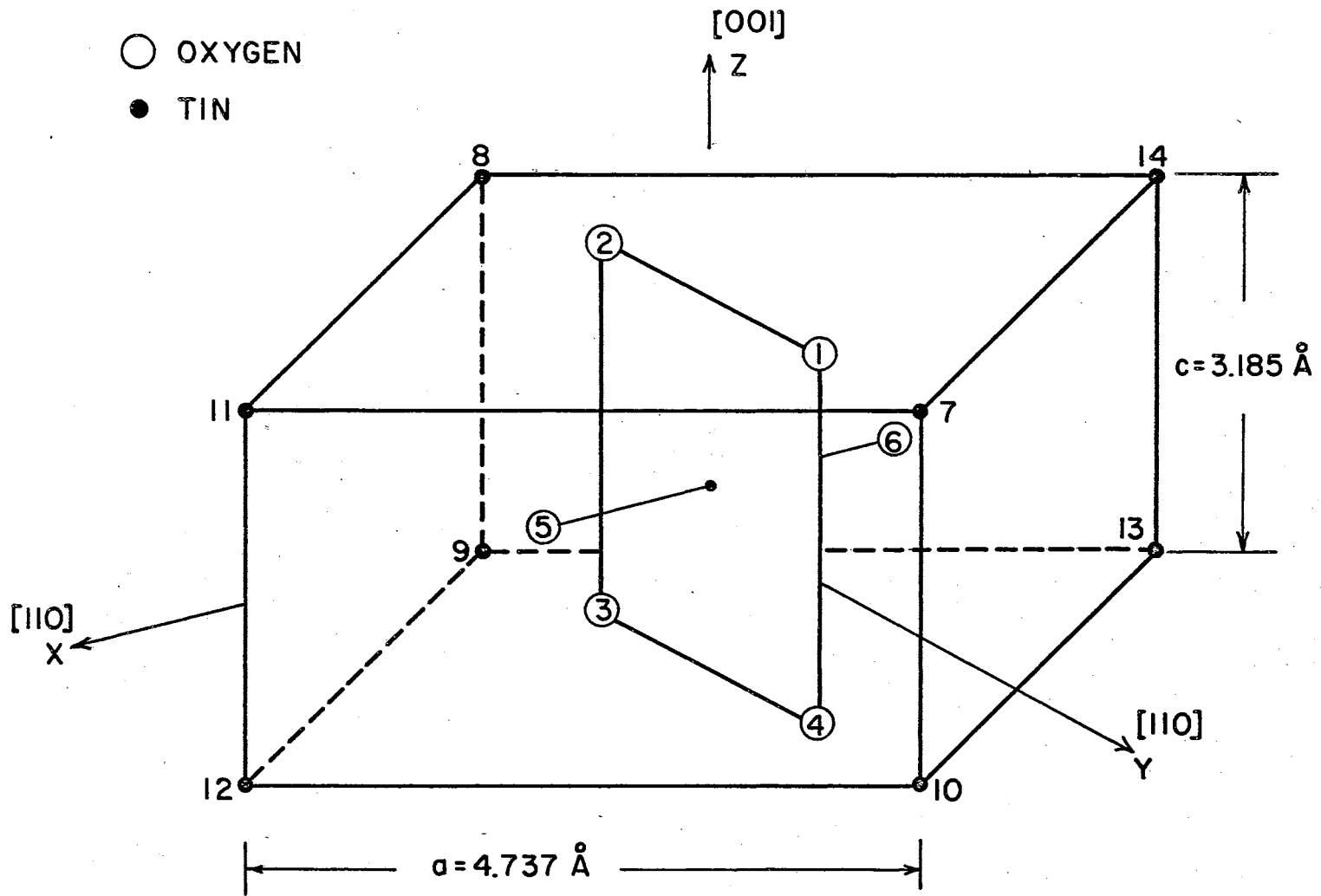


Figure 4. The Unit Cell of SnO<sub>2</sub>

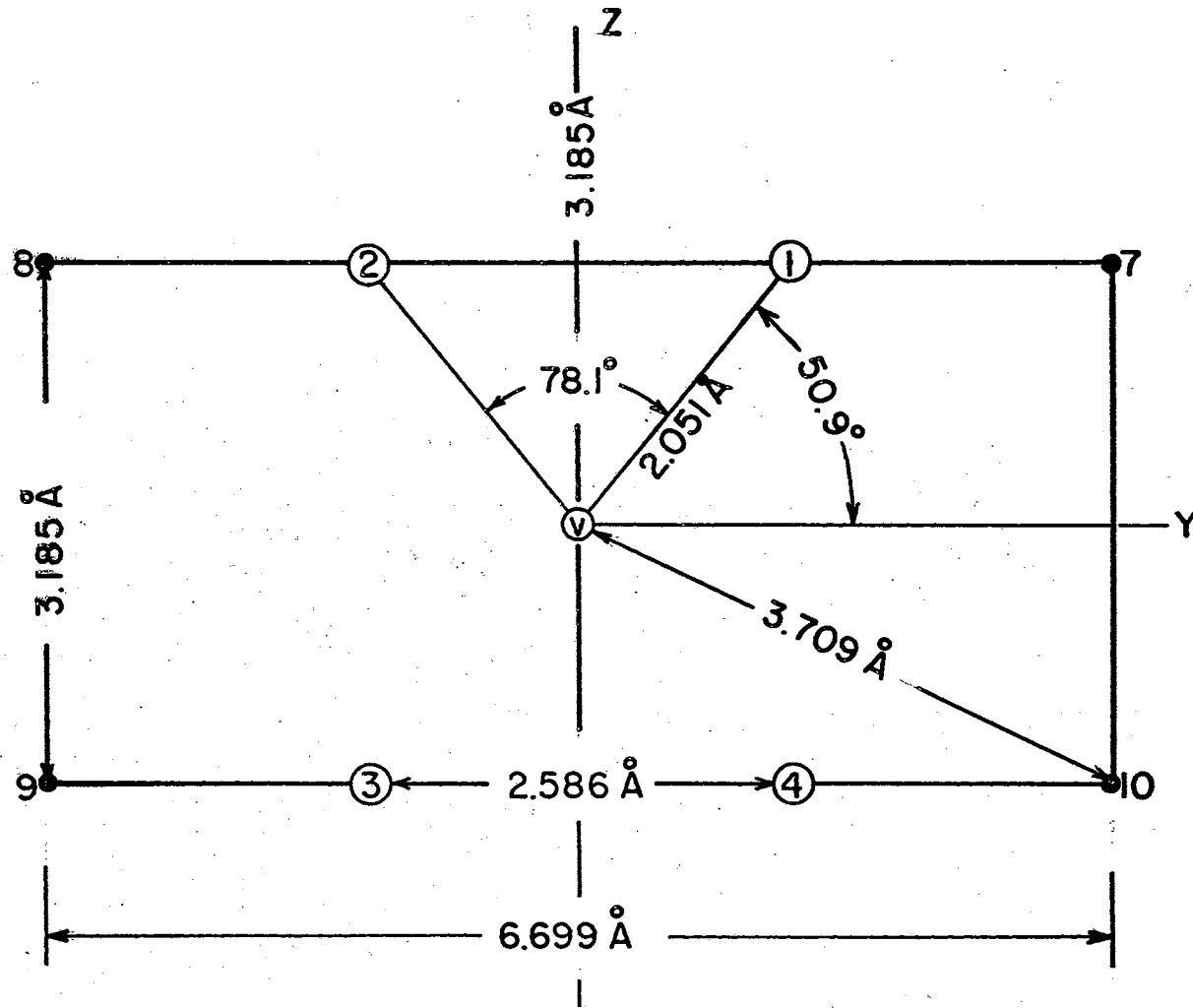


Figure 5. Unit Cell as Viewed Along the  $[110]$  Direction

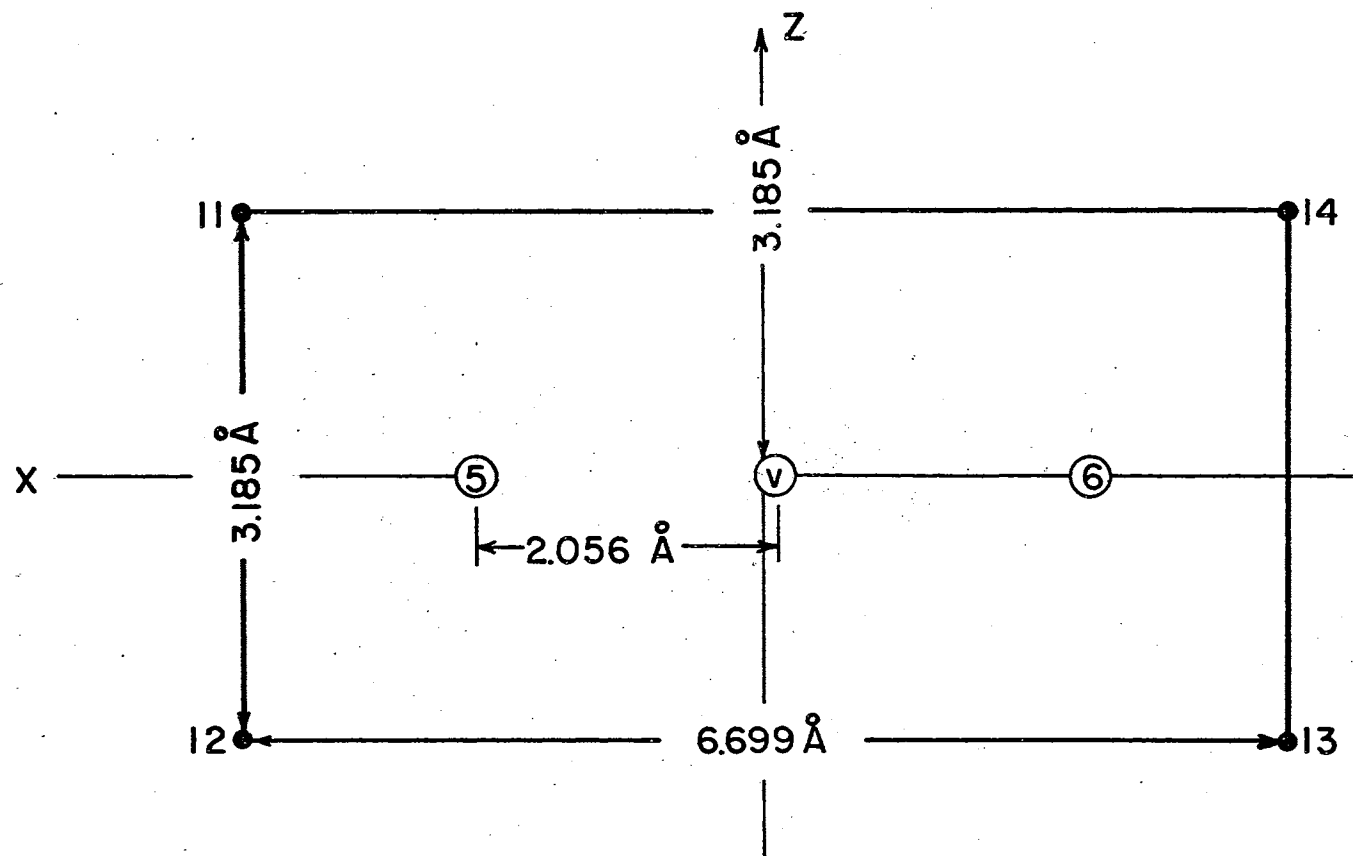


Figure 6. Unit Cell as Viewed Along the  $[1\bar{1}0]$  Direction

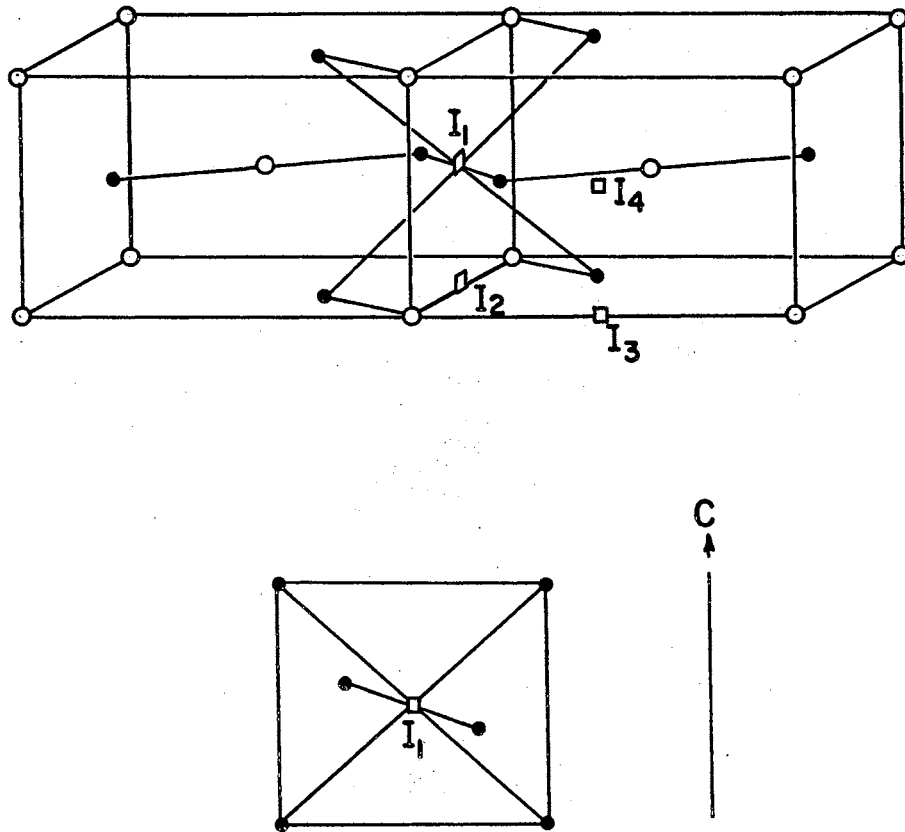


Figure 7. The Octahedrally Coordinated Interstitial Site  
in  $\text{SnO}_2$

All of the above sites of each type become magnetically equivalent along the [001] direction.



## CHAPTER IV

### RESULTS AND CONCLUSIONS CONCERNING ION STUDIES

#### Identification of the Nickel Center

The identification of the  $\text{Ni}^{3+}$  center rests on two diffusion experiments performed on crystals grown by a vapor transport process at Corning Glass Research.<sup>2</sup> These crystals, which displayed no suspected nickel signal before the treatment, gave a very significant resonance after treatment. The first diffusion treatment, carried out on sample 137-K, consisted of a diffusion of both chromium and nickel into the crystal. After pre-diffusion ESR measurements were taken (Figure 8a), the sample was placed in a small quartz capsule in the presence of a nichrome wire which had been degreased and acid cleaned. The contents were then heated in air by the use of a gas-oxygen torch until the nichrome partially oxidized to a yellow-green powder. The capsule was then placed into a quartz and glass system which allowed control of the gaseous ambient. Nitrogen was introduced into the system and the contents were heated to  $\approx 1000^{\circ}\text{C}$  for a period of one week. The nitrogen ambient was used since it would allow the introduction of oxygen vacancies into the sample (see Chapter V) and thus increase the mobility of the diffusing ions.

At the conclusion of the heat treatment in nitrogen, oxygen was admitted into the system and the sample was again heated for 8 hours

at  $\approx 1000^{\circ}\text{C}$  for the purpose of oxidizing it back to its original stoichiometry. Subsequent ESR measurements revealed two distinct differences from the measurements taken before treatment. First, the resistance was much higher as indicated by the observation of the cavity resonance during the spectrometer adjustment and operation. Comparing with other samples of similar resistances, it was estimated that the resistance increased several orders of magnitude during the treatment. Secondly, the suspected  $\text{Ni}^{3+}$  signal shown in Figure 8c (which had been seen previously in flux-grown  $\text{SnO}_2$  crystals) appeared together with an increase of the already present  $\text{Cr}^{3+}$  signals.

In preparation for the second diffusion experiment a chip was broken from sample 137-G and heat-treated in oxygen for two days. Subsequent careful ESR measurements showed again an absence of the suspected nickel signal. This sample and 137-K were dipped into a methanol-nickel acetate solution and placed in separate quartz capsules in the treatment apparatus. The apparatus was evacuated allowing the methanol to evaporate and the contents were heated to decompose the acetate leaving a nickel oxide residue on the crystal surface.<sup>36</sup> The previously described nitrogen treatment was then applied for two weeks followed by a two-day similar treatment in oxygen. ESR measurements carried out on these samples gave the characteristic results to be expected on the basis of the previous experiment on 137-K. The suspected nickel signal increased fourfold in 137-K as shown in Figure 8e. The chip from 137-G also displayed a very distinct suspected nickel signal together with a resistance increase. The resistance increase, however, was not so obvious in this case because of the much smaller sample size.

From these two experiments it was concluded that the ESR signal

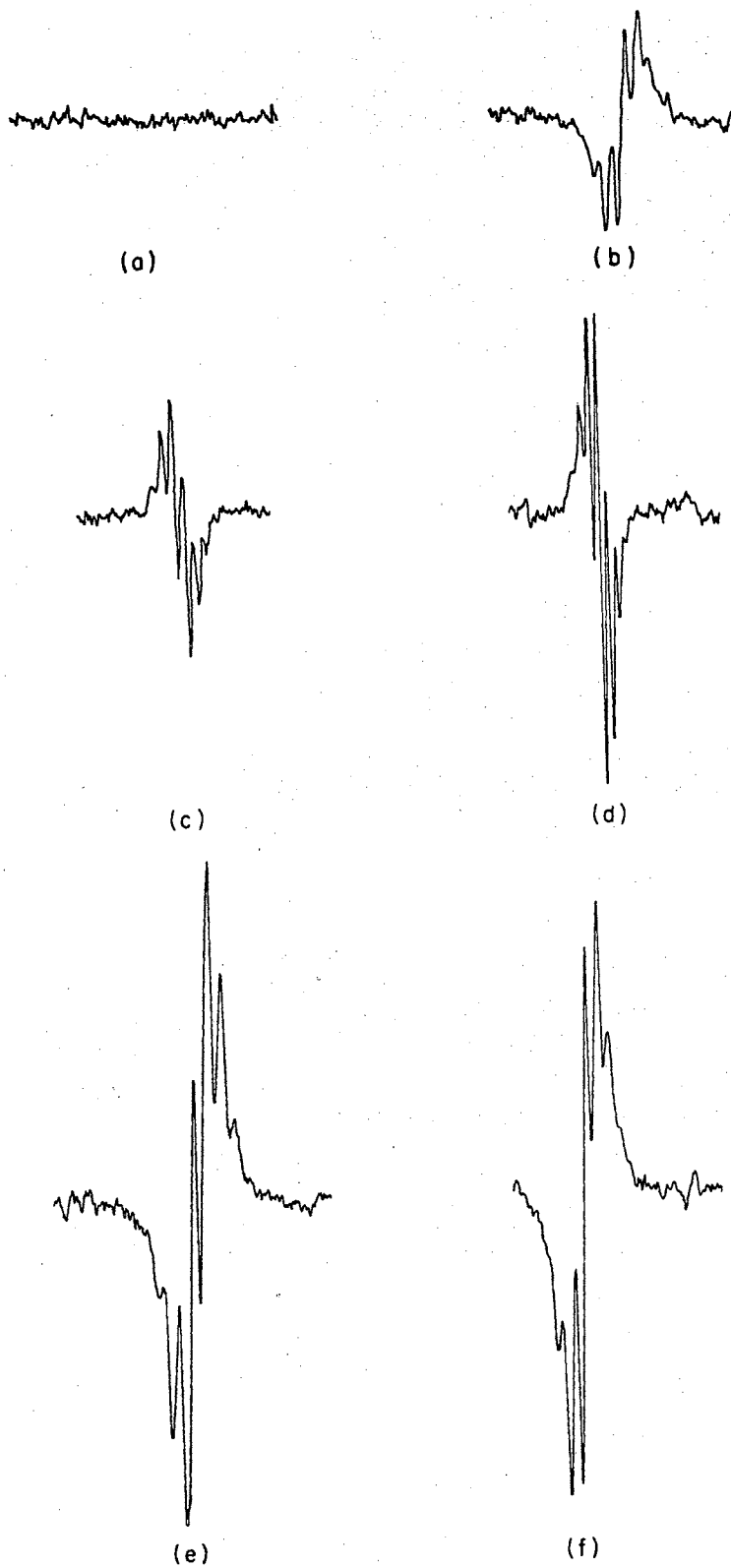


Figure 8. Comparison of the Signal due to  $\text{Ni}^{3+}$ : (a) Before Diffusion, (b) After First Diffusion and (c) After Second Diffusion, With the Corresponding  $\text{Fe}^{3+}$  Signals (b), (d) and (e)

found in flux-grown stannic oxide and induced in vapor-grown stannic oxide is due to a nickel center.

#### Orientation Dependence of the Nickel Spectrum

The orientation dependence of the observed nickel signal is shown in Figure 9. Since the nature of the signal indicates a fourfold symmetry exists for the site of this ion, only a  $90^\circ$  interval is shown although measurements over a larger angle were taken. As can be seen, there are four magnetically inequivalent sites which decrease to two in the  $[110]$ ,  $[\bar{1}\bar{1}0]$  and  $[100]$  directions. From this it can be concluded that the nickel probably occupies the distorted octahedral interstitial position discussed in the previous chapter. It should be recognized, however, that a substitutional site distorted in a very special way might also explain these results. The type of distortion required seems highly improbable.

Using equation 13 for an effective spin  $S = \frac{1}{2}$ ,

$$W = 3H_0 \sqrt{g_x^2 \sin^2 \theta \cos^2 \phi + g_y^2 \sin^2 \theta \sin^2 \phi + g_z^2 \cos^2 \theta} \quad (34)$$

the parameters  $g_x$ ,  $g_y$  and  $g_z$  were calculated. Since  $w$  is known from the microwave frequency, this was easily done using the values for  $H_0$  along the magnetic  $x$ ,  $y$  and  $z$  axes shown in Figures 9 and 10. It is noted that two of the terms under the square root are zero for each of these values allowing easy solution for the appropriate spectroscopic splitting factor. As one can see from Figures 10 and 11, the orientation dependence fit is extremely good. Thus, the effective spin has been taken as  $S = \frac{1}{2}$  with the spectroscopic splitting factors given by:

$$g_x = 1.96, \quad g_y = 5.10 \quad \text{and} \quad g_z = 6.84.$$

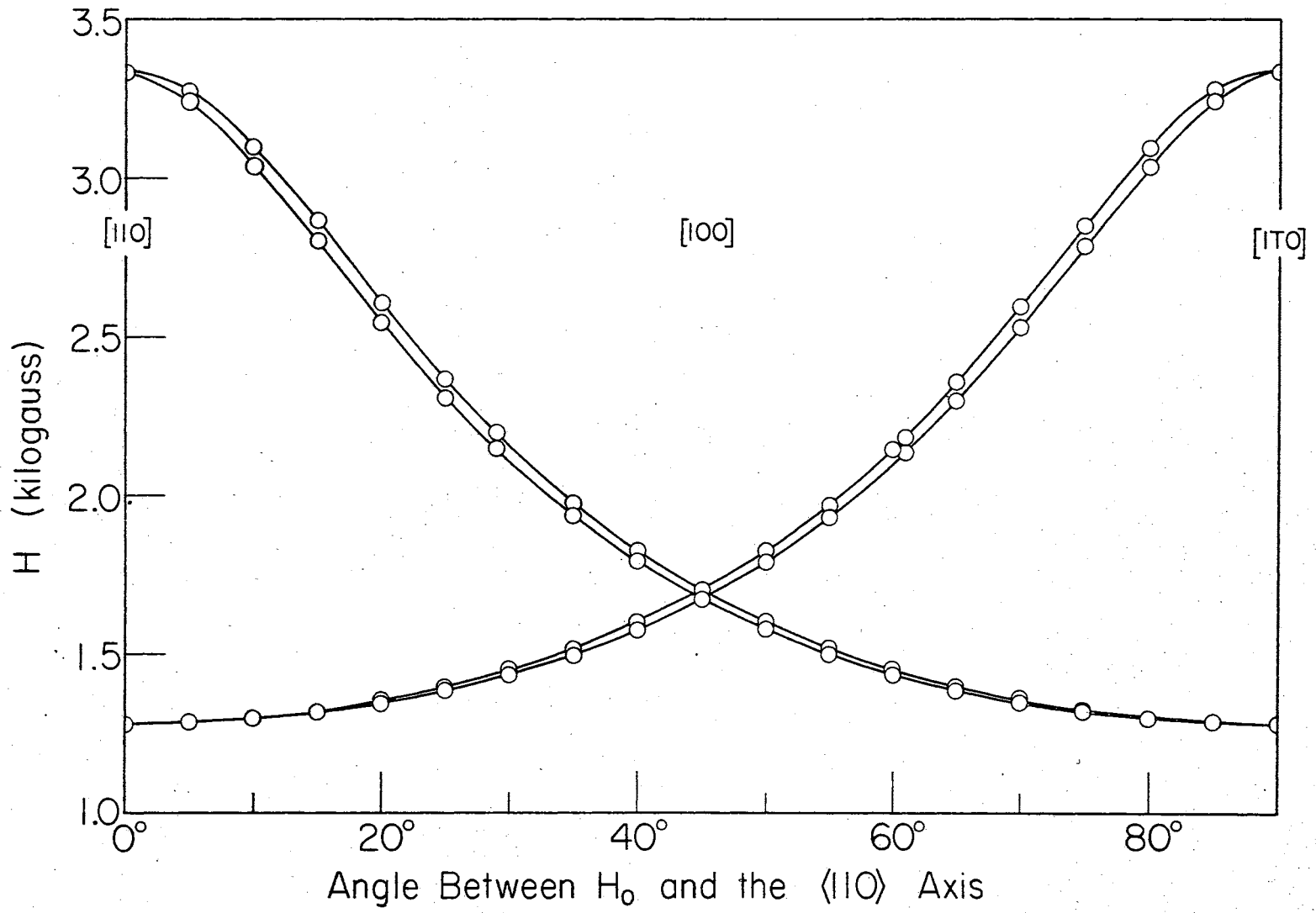


Figure 9. Observed Resonances of  $\text{Ni}^{3+}$  in the X-Y Plane

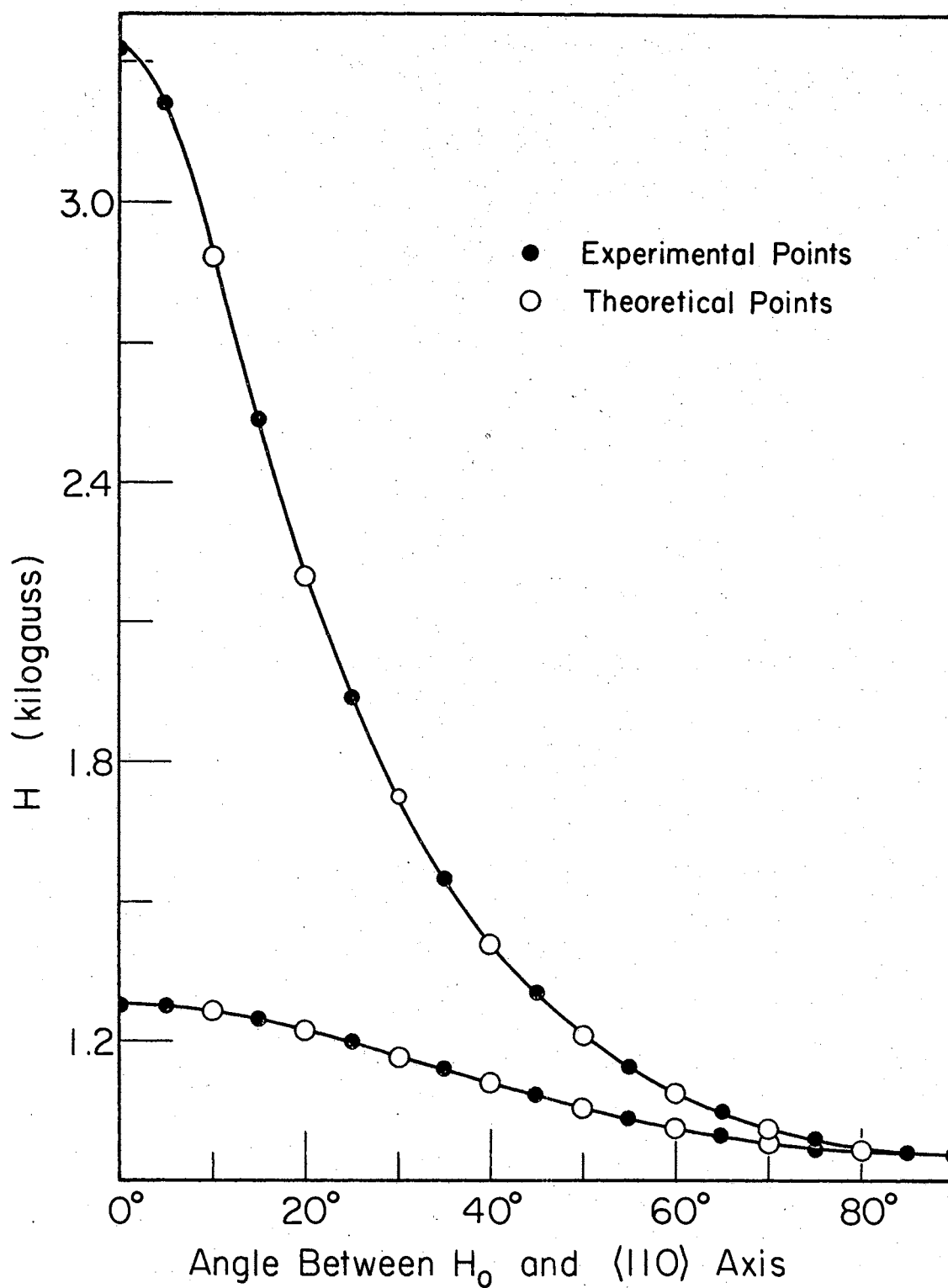


Figure 10. Observed and Calculated Resonances of  $\text{Ni}^{3+}$  in the X-Z and Y-Z

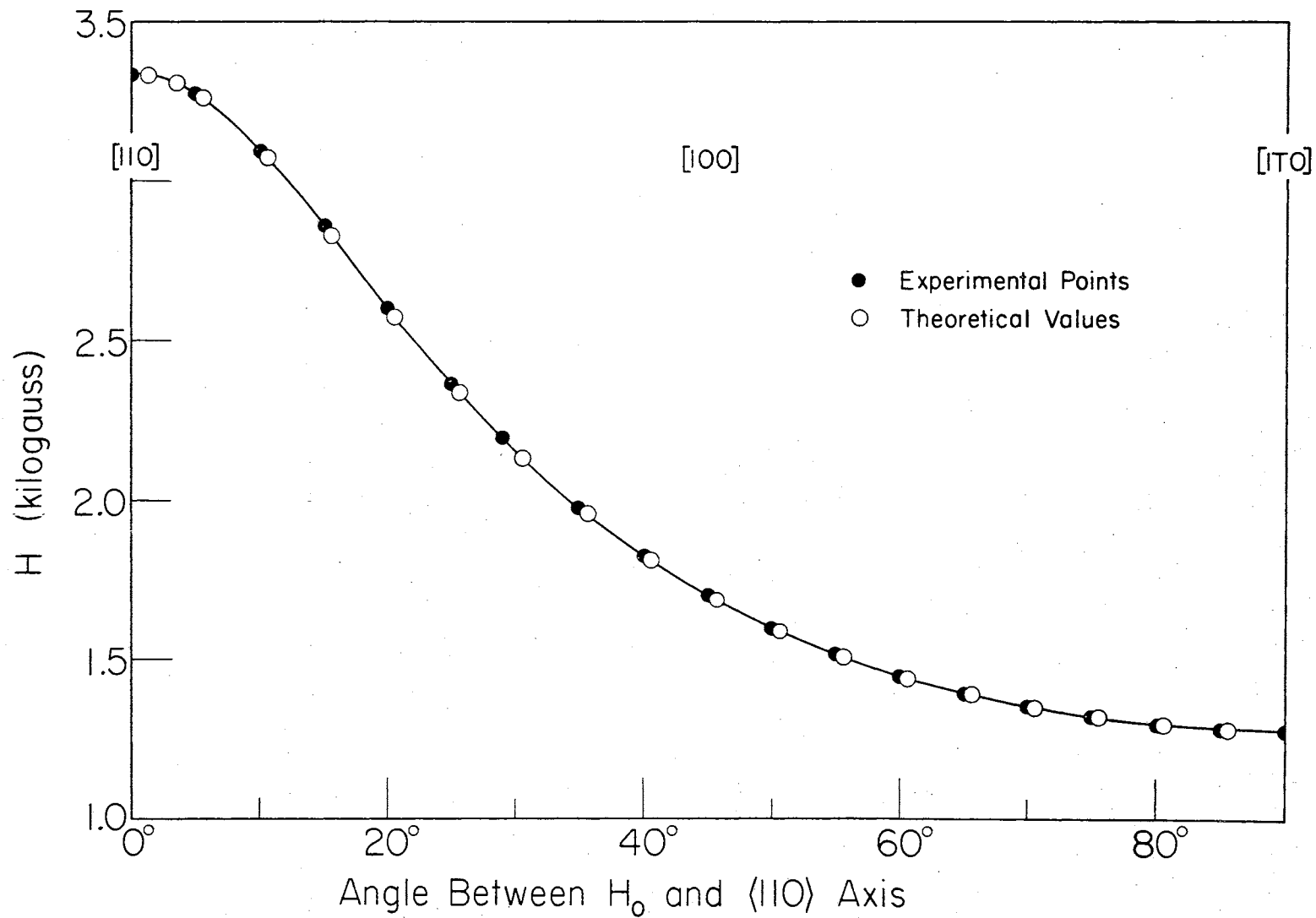


Figure 11. Observed and Calculated Resonances of  $Ni^{3+}$  in the X-Y Plane

The valency is easily determined if one considers the data from similar systems. The nickel ion which would most plausibly give  $S = \frac{1}{2}$  and such large g-values<sup>38-45</sup> is the  $\text{Ni}^{3+} d^7$  system. The  $d^7$  system most widely investigated is that of  $\text{Co}^{2+}$  in various materials. Here, too, large anisotropic g-values are observed. The only other system which might give  $S = \frac{1}{2}$  would be the  $\text{Ni}^{1+} d^9$  system. This system, however, would not be expected to produce the large anisotropic observed g-values.<sup>46,47</sup> Thus it has been chosen to identify the center as a  $\text{Ni}^{3+}$  ion in an interstitial site.

From Figure 9 one can see that two of the magnetic axes of the  $\text{Ni}^{3+}$  system do not correspond to the  $[110]$  and  $[1\bar{1}0]$  axes of the crystal, but rather lie  $\pm 0.6^\circ$  from these principal directions. This is not surprising since the previously identified  $\text{Cr}^{3+}$  interstitial impurity has been reported to have magnetic axes which point  $\pm 0.5^\circ$  from the  $[110]$  and  $[1\bar{1}0]$  directions.<sup>11</sup>

One can explain this behavior by considering the arrangement of nearest neighbor oxygen and tin atoms. The nearest neighbor oxygen atoms form a distorted octahedron with the tetragonal axis in the  $\{001\}$  plane at an angle of  $13^\circ$  from the  $[110]$  axis. On the other side of the  $[110]$  axis at an angle of  $45^\circ$  in the same plane lies the tetragonal axis of another distorted octahedron formed by the nearest neighbor tin ions. The magnetic axis is then expected to lie somewhere between these two directions. Since the  $\text{Ni}^{3+}$ -oxygen interaction is expected to be the stronger of the two, one expects the magnetic axis to be closer to the oxygen tetragonal axis, which is in qualitative agreement with the observed results.

In the analogous case of  $\text{Ni}^{3+}$  in  $\text{TiO}_2$  one might expect the magnetic



axis to lie even nearer the oxygen tetragonal axis. This is because superhyperfine structure observations<sup>10,37</sup> indicate a larger amount of covalency in  $\text{SnO}_2$  than in  $\text{TiO}_2$ . Again the expectation is fulfilled since the magnetic axis lies at an angle of  $5.4^\circ$  from the  $[110]$  direction for this case.<sup>38</sup>

### Crystal Field Effects on $\text{Ni}^{3+}$ in Stannic Oxide

The splitting of the  $d^7$  ground state has been considered by several authors<sup>14,39</sup> for the case of  $\text{Co}^{2+}$ . Only the most qualitative calculations will be made in an effort to point out possible interpretations of the observed  $g$ -values in the  $\text{Ni}^{3+} d^7$  system.

The ground state of the  $\text{Ni}^{3+}$  ion of  $d^7$  configuration according to Hund's rules is a  $^3/2_F$  state. Thus for the free ion case a sevenfold orbital degeneracy exists together with a fourfold spin degeneracy. If we consider--as described in Chapter II--a series of perturbations caused by the  $\text{SnO}_2$  host, the largest will obviously be the reduction of symmetry from spherical to octahedral due to the nearest neighbor oxygen atoms. Using equation 25 to break the reducible representation  $D^{(3)}$  by use of the characters given in Table III into the irreducible representations of the full octahedral  $O_h$  group, one obtains

$$D^{(3)} = \Gamma_4^- \quad \Gamma_5^- \quad \Gamma_2^- \quad . \quad (35)$$

Thus the sevenfold orbital degeneracy breaks into two orbital triplets and an orbital singlet. The separations of these manifolds will be approximately the same as those for  $\text{Co}^{2+}$  and for this reason the model proposed by Low<sup>39</sup> for  $\text{Co}^{2+}$  in  $\text{MgO}$  is given in Figure 12.

It is rather hard to decide a priori which perturbation should be

TABLE III  
CHARACTER TABLE FOR  $O_h$  SYMMETRY GROUP

Representation	E	$8C_3(8)$	$3C_4^2$	$6C_2$	$6C_4$	I	$8S_6$	$3\sigma_h$	$6\sigma_d$	$6S_4$
$\Gamma_1^+$	1	1	1	1	1	1	1	1	1	1
$\Gamma_1^-$	1	1	1	1	1	-1	-1	-1	-1	-1
$\Gamma_2^+$	1	1	1	-1	-1	1	1	1	-1	-1
$\Gamma_2^-$	1	1	1	-1	-1	-1	-1	-1	1	1
$\Gamma_3^+$	2	-1	2	0	0	2	-1	2	0	0
$\Gamma_3^-$	2	-1	2	0	0	-2	1	-2	0	0
$\Gamma_4^+$	3	0	-1	-1	1	3	0	-1	-1	1
$\Gamma_4^-$	3	0	-1	-1	1	-3	0	1	1	-1
$\Gamma_5^+$	3	0	-1	1	-1	3	0	-1	1	-1
$\Gamma_5^-$	3	0	-1	1	-1	-3	0	1	-1	1
$D^{(3)}$	7	1	-1	-1	-1	-7	-1	1	1	1

carried out next, however. One would expect the spin orbit interaction to be a few hundred inverse centimeters; nevertheless, the distortions due to both the deviation from octahedral symmetry of the surrounding oxygen ions, and interactions with the nearest neighbor tin ions could easily be that large. For the sake of simplicity, consider only the result of spin orbit interaction in cubic symmetry on the  ${}^4\Gamma_4^-$  manifold and ignore interactions with the  ${}^4\Gamma_5^-$  and  ${}^4\Gamma_2^-$  manifolds since these would give only small contributions to the g-value (approximately 0.16).

Since the net spin of the  $\text{Ni}^{3+}$  system is  $\frac{3}{2}$ , the spin part of the wavefunction will transform as the  $D^{(3/2)}$  representation. The product of the spin and orbital parts of the  ${}^4\Gamma_4^-$  manifold will then transform as the direct product  ${}^4\Gamma_4^- \times D^{(3/2)}$ . The characters of the total representation shown in Table IV can be found by equation 30. The results are then given in this same table as  $\Gamma_{\pm}$ . Applying equation 25 one obtains the result

$$\Gamma_{\pm} = \Gamma_6^- + \Gamma_7^- + 2\Gamma_8^- . \quad (36)$$

Thus the degeneracy of twelve present in the  ${}^4\Gamma_4^-$  manifold under spin orbit perturbation splits into two doublets and two fourfold degenerate levels. This splitting, as shown by Low<sup>14</sup>, is given in Figure 12. Since the spin-orbit interaction for the free ion  ${}^{48}\text{Ni}^{3+}$  is  $-238 \text{ cm}^{-1}$ , the separation between the  $\Gamma_6^-$ , Kramers doublet and the other levels is large with respect to the microwave energy ( $\approx 0.3 \text{ cm}^{-1}$ ). Thus the spin resonance may be given<sup>14</sup> by the effective spin  $S' = \frac{1}{2}$ , and one might expect the Hamiltonian of the form of equation 12 to fit the experimental data. From the comparisons of the orientation data as calculated on this basis and as determined experimentally shown in Figures 10 and

TABLE IV  
 CHARACTER TABLE FOR THE GROUP  $O_h$  DOUBLE GROUP

$O_h$	E	$\bar{E}$	$8C_2$	$8C_3$	$3C_2$ $3C_2$	$6C_4$	$6C_4$ $6C_4$	$6C_2^1$ $6C_2^1$	I	$\bar{I}$	$8S_6$	$8S_6$	$3C_2$ $3C_2$	$6S_4$	$6S_4$	$6\sigma_d$ $6\sigma_d$
$\Gamma_1^+$	1	1	1	1	1	1	1	1	1	1	1	1	1	1	1	1
$\Gamma_2^+$	1	1	1	1	1	-1	-1	-1	1	1	1	1	1	-1	-1	-1
$\Gamma_3^+$	2	2	-1	-1	2	0	0	0	2	2	-1	-1	2	0	0	0
$\Gamma_4^+$	3	3	0	0	-1	1	1	-1	3	3	0	0	-1	1	1	-1
$\Gamma_5^+$	3	3	0	0	-1	-1	-1	1	3	3	0	0	-1	-1	-1	1
$\Gamma_1^-$	1	1	1	1	1	1	1	1	-1	-1	-1	-1	-1	-1	-1	-1
$\Gamma_2^-$	1	1	1	1	1	-1	-1	-1	-1	-1	-1	-1	-1	1	1	1
$\Gamma_3^-$	2	2	-1	-1	2	0	0	0	-2	-2	1	1	-2	0	0	0
$\Gamma_4^-$	3	3	0	0	-1	1	1	-1	-3	-3	0	0	1	-1	-1	1
$\Gamma_5^-$	3	3	0	0	-1	-1	-1	1	-3	-3	0	0	1	1	1	-1
$\Gamma_6^+$	3	3	0	0	-1	-1	-1	1	-3	-3	0	0	1	1	1	-1
$\Gamma_7^+$	2	-2	1	-1	0	-2	2	0	2	-2	1	-1	0	-2	2	0
$\Gamma_8^+$	4	-4	-1	1	0	0	0	0	4	-4	-1	1	0	0	0	0
$\Gamma_6^-$	2	-2	1	-1	0	2	-2	0	-2	2	-1	1	0	-2	2	0
$\Gamma_7^-$	2	-2	1	-1	0	-2	2	0	-2	2	-1	1	0	2	-2	0
$\Gamma_8^-$	4	-4	-1	1	0	0	0	0	-4	4	1	-1	0	0	0	0
$\Gamma_{3/2}^+$	4	-4	-1	1	0	0	0	0	+4	-4	-1	+1	0	0	0	0
$\Gamma_{\pm}$	12	-12	0	0	0	0	0	0	-12	+12	0	0	0	0	0	0

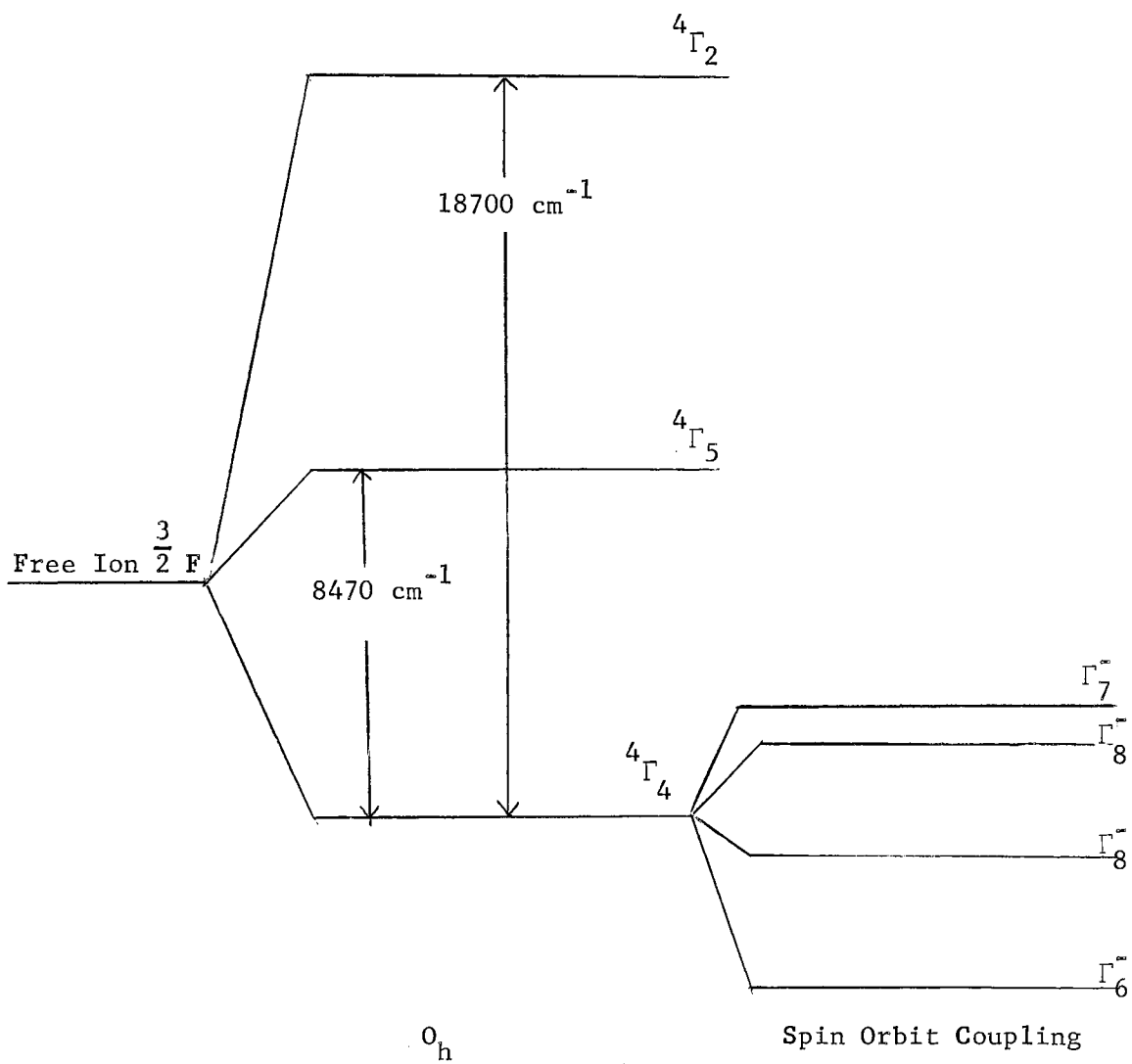


Figure 12. Splitting of the  $\text{Co}^{2+}$  Ground State in  $\text{MgO}$

11, one would conclude that although other perturbations may be comparable to the spin orbit interaction, the  $\Gamma_6^-$  doublet probably stays removed from the other levels by a large energy with respect to the incident microwave energy.

A theoretical calculation of actual magnitudes for g-values is much more difficult than just predicting their orientation dependence as was done above.

No theoretical treatment in the literature to date applies directly to the problem of  $C_{2h}$  symmetry which is pertinent to the case at hand. However, calculations for more symmetrical configurations have been made. A simple theoretical perturbation calculation by Low carried out for a  $Co^{2+}$  ion in cubic symmetry, assuming only electrostatic interaction, gives a g-value of 4.333 for the ground state of the  $4\Gamma_4^-$  manifold.<sup>14</sup> An extension of this calculation to tetragonal symmetry by Abragam and Pryce<sup>40</sup> gave a curve relating  $g_{11}$  to  $g_{\perp}$  of the form shown in Figure 3. If distortions from this symmetry are small, one could for comparison simply draw a vertical line at  $g_{11} = 6.85$  and then  $g_x$

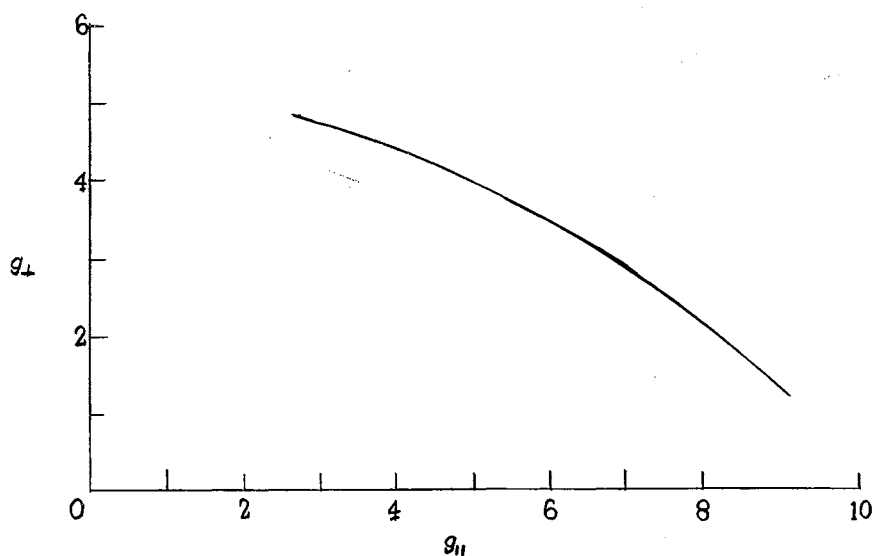


Figure 13. Splitting Factors--Trigonal Symmetry

and  $g_y$  should lie equal distances from the intersection of this line and the Abragam-Pryce curve. As one can see, this is only approximately true for the  $Ni^{3+}$  data.

A further extension by Tinkham<sup>41</sup> for the case of rhombic symmetry where covalency was incorporated into an orbital reduction factor gave the relations

$$\begin{aligned} g_x &= \left(\frac{10}{3} - \frac{8}{3} a\right) + K (1-2a) \\ g_y &= \left(\frac{10}{3} + \frac{4}{3} a + \frac{4}{3} r\right) + K (1+a+r) \\ g_z &= \left(\frac{10}{3} + \frac{4}{3} a - \frac{4}{3} r\right) + K (1+a-r). \end{aligned} \quad (37)$$

Solving these equations using  $Ni^{3+}$  experimental g-values, one gets the constants  $K = 1.3$ ,  $a = 0.5$  and  $r = 0.36$ . Although the values of  $a$  and  $r$  are qualitatively logical in view of the values  $a = 0.45$  and  $r = 0.55$  found for  $Co^{2+}$  in  $TiO_2$ , the calculated value of  $K$  is obviously in error since  $K = 1$  signifies complete ionic character.

#### Superhyperfine Structure of $Ni^{3+}$

The characteristic line shapes of the  $Ni^{3+}$  signals are shown in Figures 14-17. From these it is evident that a prominent superhyperfine interaction exists for all orientations other than  $H_0$  parallel to the magnetic x-axis. Although a detailed study of the anisotropy in this structure would require a crystal doped with many more  $Ni^{3+}$  centers, an approximate value of 6 gauss for the superhyperfine splitting may be measured from the displayed data. This is very close to the values reported<sup>11</sup> for the  $Cr^{3+}$  interstitial ion, and thus the small deviation ( $0.1^\circ$ ) in the directions of the magnetic x and y axes for these two ions is understandable.

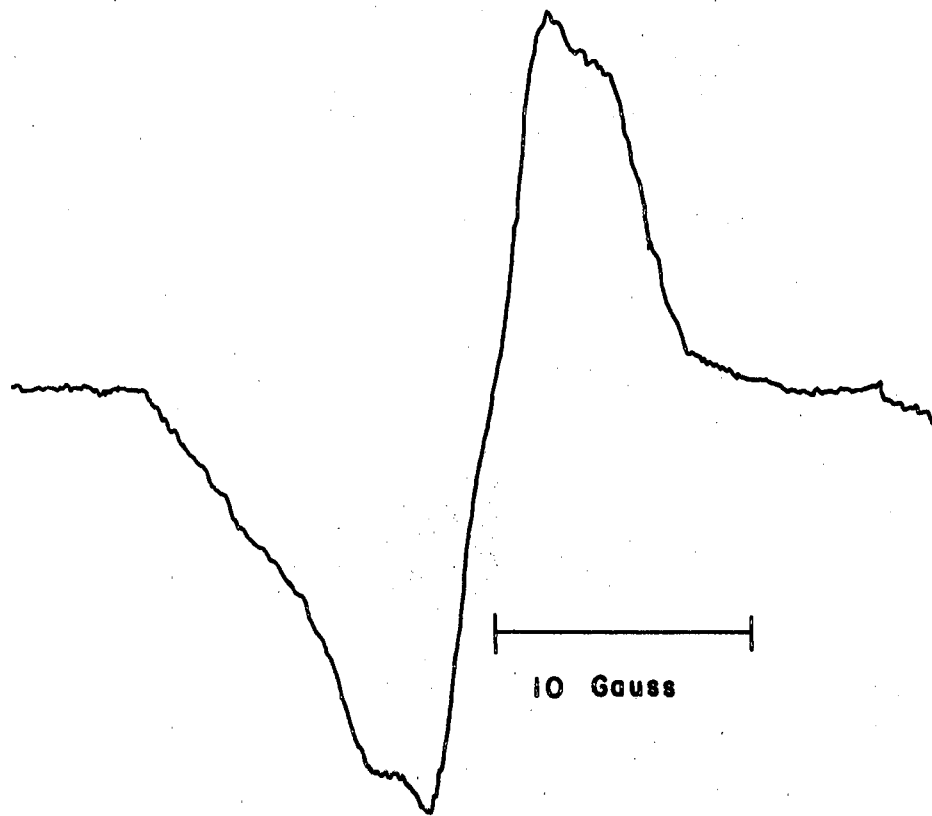


Figure 14. Resonance of  $\text{Ni}^{3+}$  for  $H_0$  Parallel to the X-axis



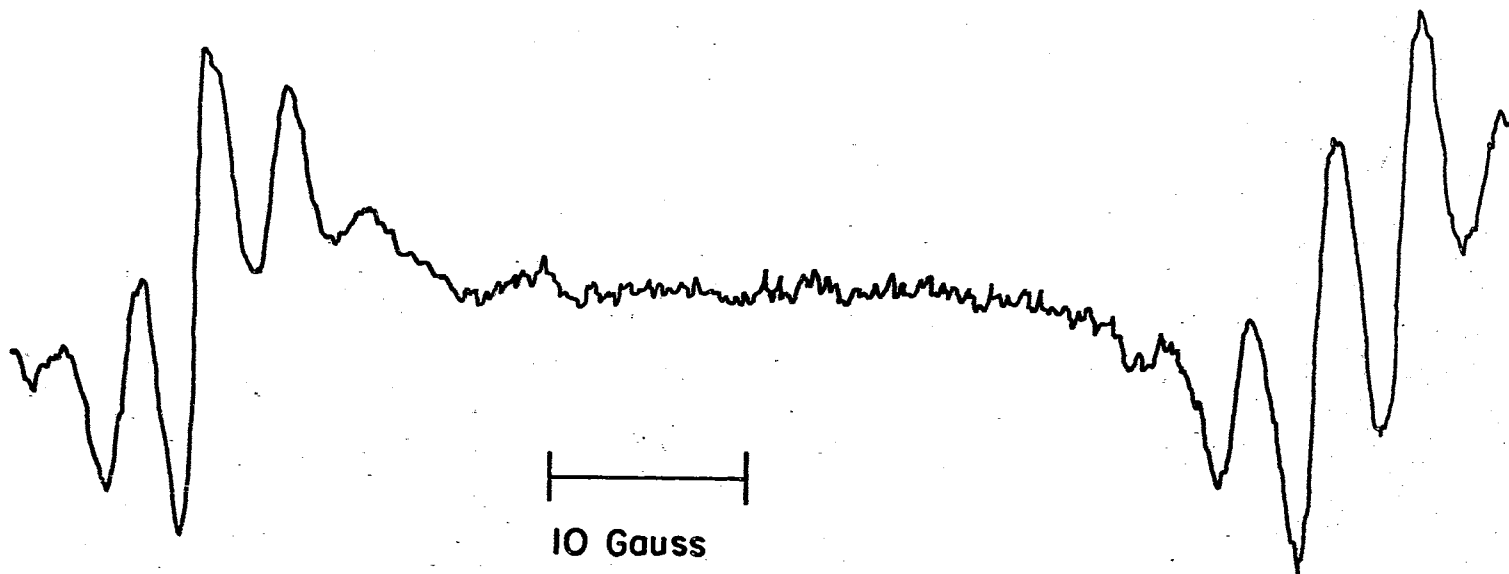


Figure 15. Resonance of Ni<sup>3+</sup> for H<sub>0</sub> 10<sup>0</sup> From the X-axis in the {001} Plane

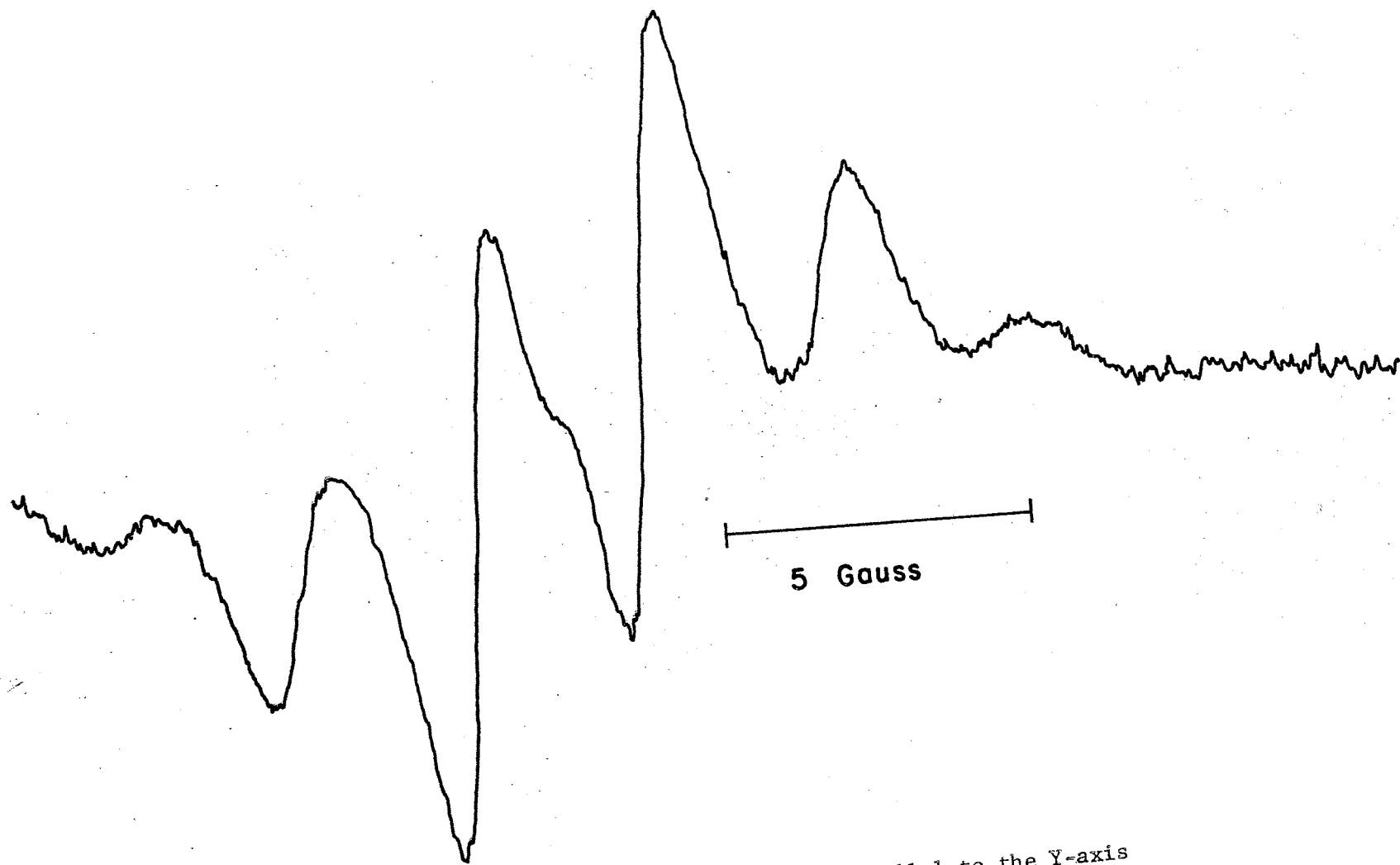


Figure 16. Resonance of Ni<sup>3+</sup> for H<sub>0</sub> Parallel to the Y-axis

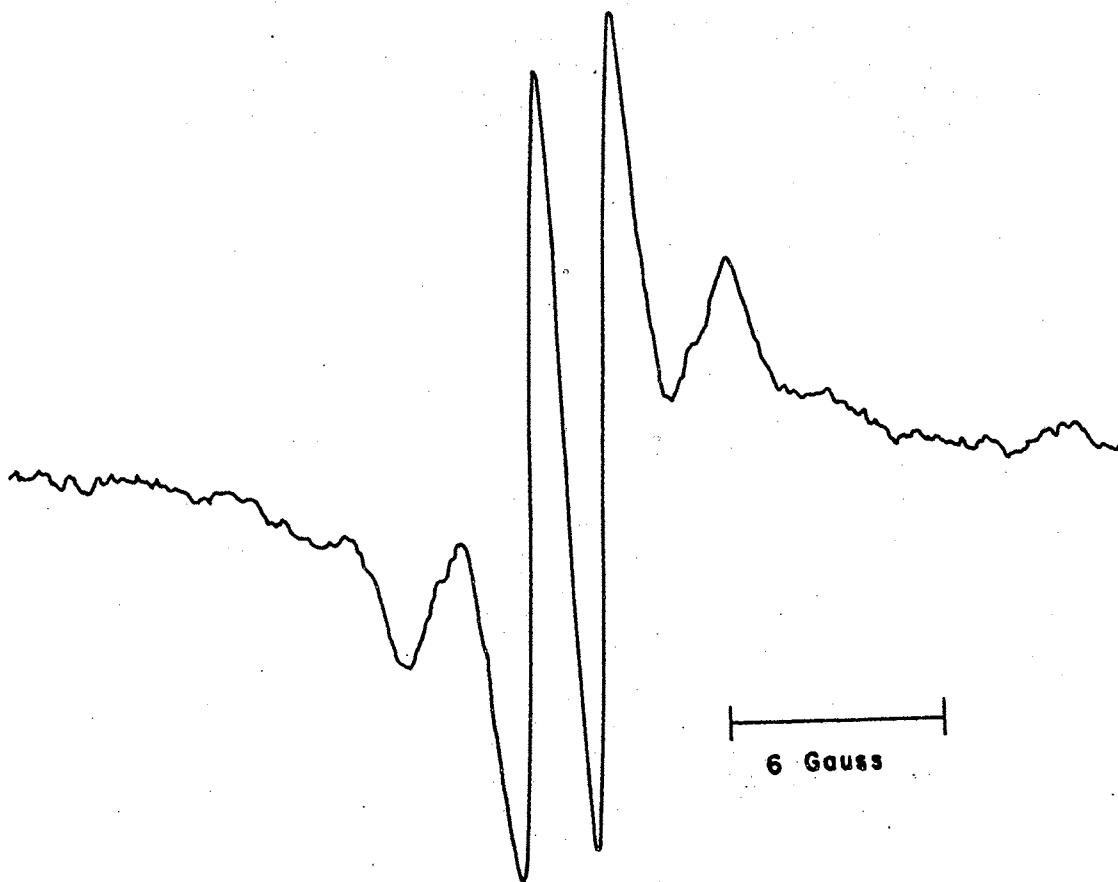


Figure 17. Resonance of Ni<sup>3+</sup> for H<sub>0</sub> Parallel to the Z-axis

ESR of  $\text{Cr}^{3+}$  in Flux-Grown  $\text{SnO}_2$ 

Electron spin resonance measurements of  $\text{Cr}^{3+}$  in vapor-grown  $\text{SnO}_2$  have been reported at K,  $K_A^{10}$ , and X-band<sup>11</sup> frequencies. Since the rather complete analysis of X-band work appeared during the course of this study, only a very limited analysis was made of the data obtained on flux-grown specimens. The main emphasis was in the identification of the center, the counting of the number of centers, and the observation of heat treatment effects on these centers which will be discussed later.

Identification of these ions was easily made after the study by Hou et. al.<sup>11</sup> Assuming a linear frequency conversion, their data taken at 9.5 KMc could be directly compared with those of this study which were taken at 9.13 KMc. Figures 18-21 show the orientation data which were taken in this study and used in the comparison. One can also use the line shapes shown in Figures 22 and 23 to help substantiate the identity.

Additional support for attributing the signals to  $\text{Cr}^{3+}$  came also with the first doping of 137-K described previously. In this process, when 137-K was heated in the presence of both chromium and nickel oxides), an increase in the  $\text{Cr}^{3+}$  signals was observed.

Detailed study of the  $\text{Cr}^{3+}$  ions in flux-grown specimens was hampered by the small number of chromium centers present in the crystals (see Table VI). This prohibited investigation of the superhyperfine structure at small modulation fields, and leads one to expect that observed line shapes are slightly distorted. Also, with one exception Figure 19, only the  $\pm\frac{1}{2}$  allowed transition was observed. Further doping

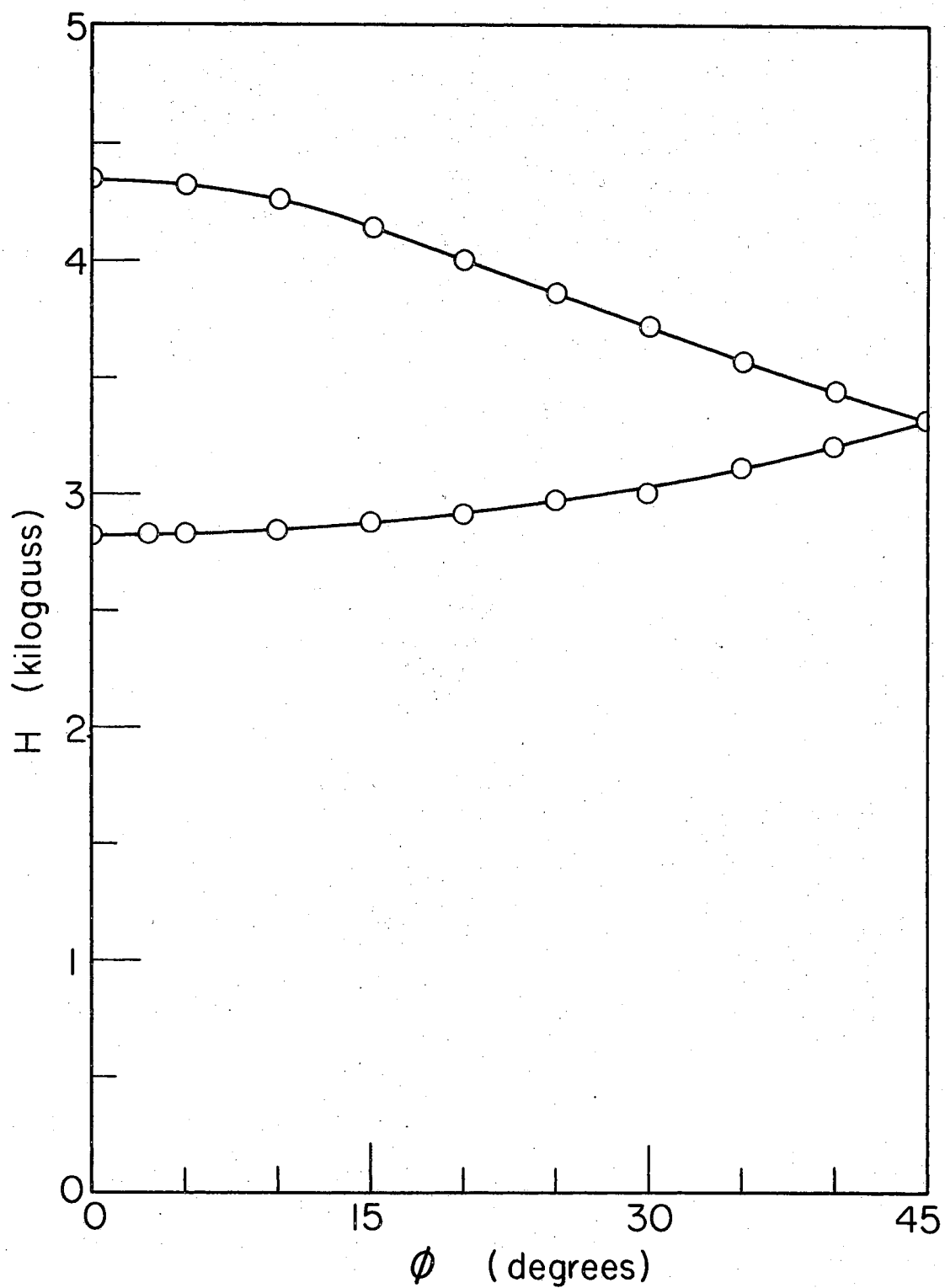


Figure 18. Orientation Dependence in the {001} Plane of Substitutional  $\text{Cr}^{3+}$  ESR Signal

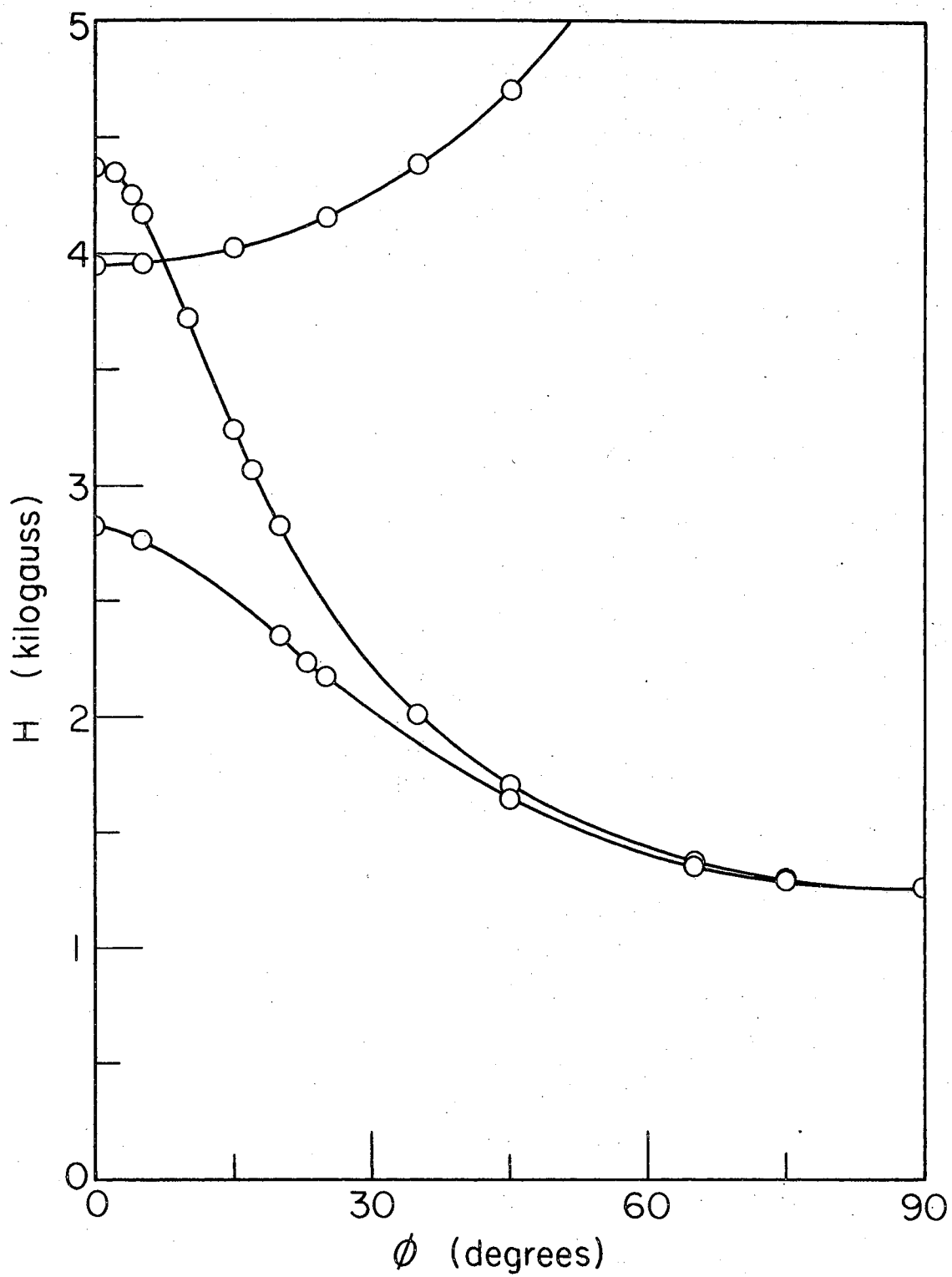


Figure 19. Orientation Dependence in the  $\{110\}$  Plane of Substitutional  $\text{Cr}^{3+}$  ESR Signal

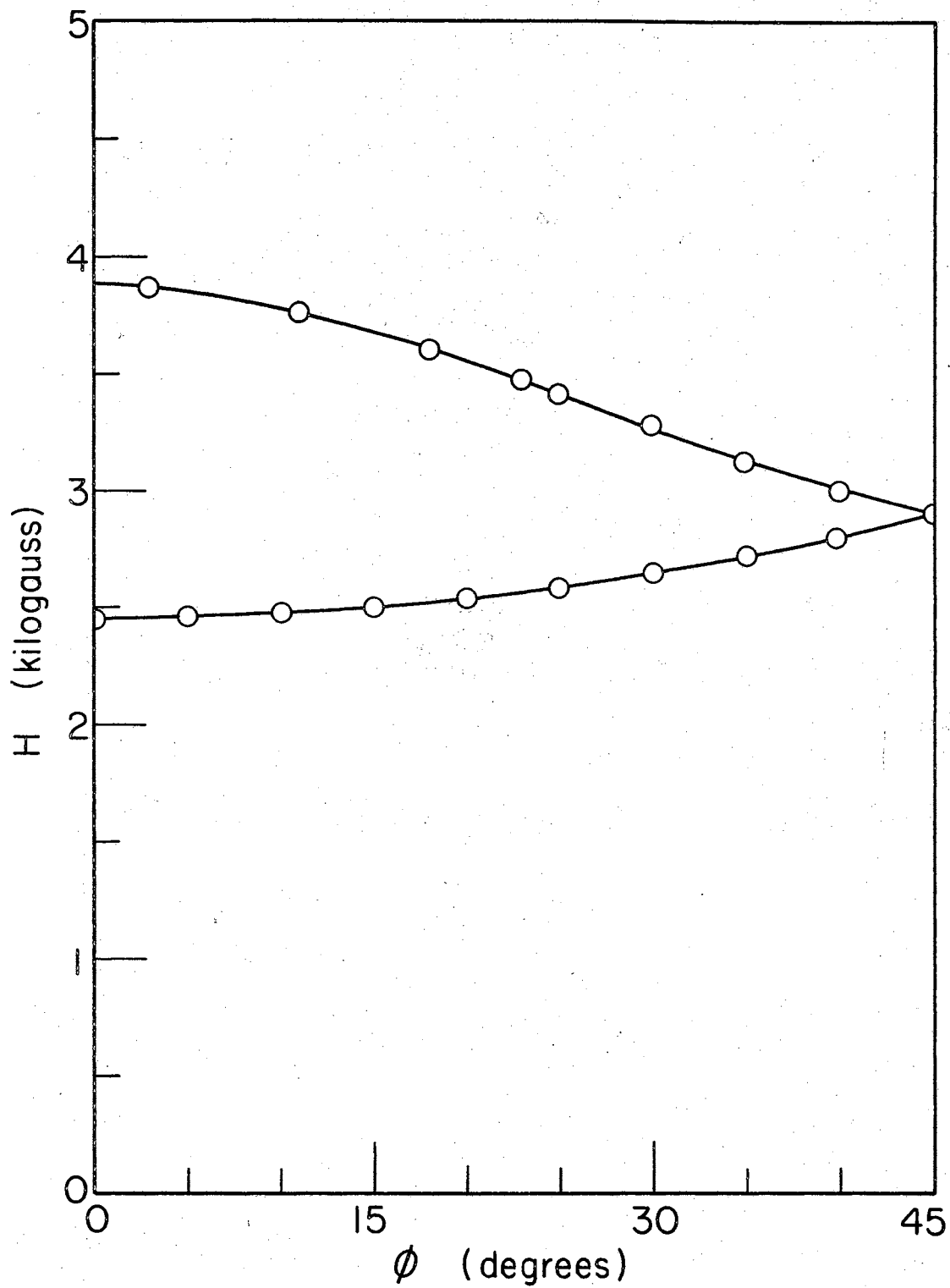


Figure 20. Orientation Dependence of Interstitial  $\text{Cr}^{3+}$  ESR Signal in the  $\{001\}$  Plane

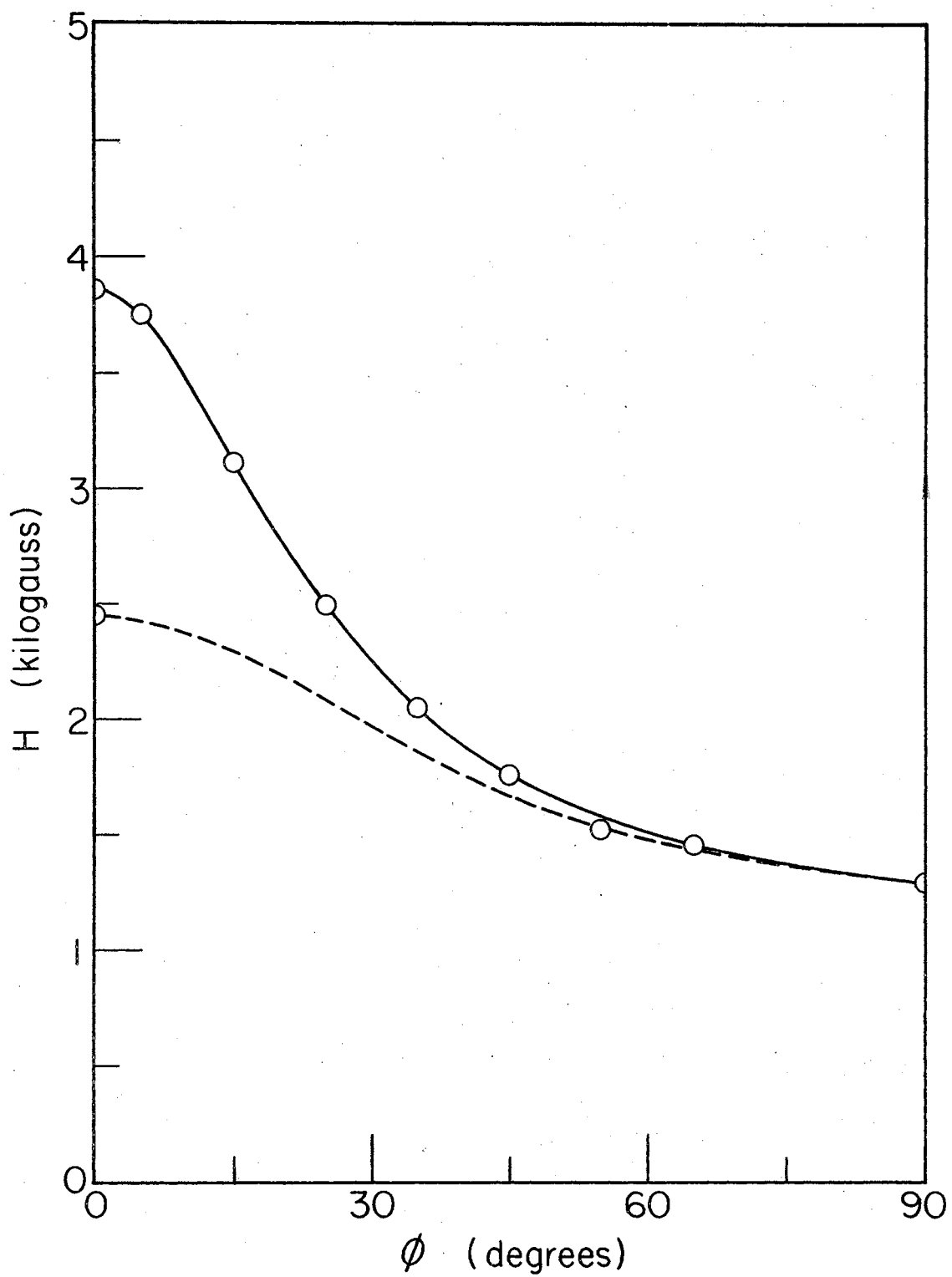


Figure 21. Orientation Dependence of Interstitial  $\text{Cr}^{3+}$  ESR Signal in the  $\{110\}$  Plane



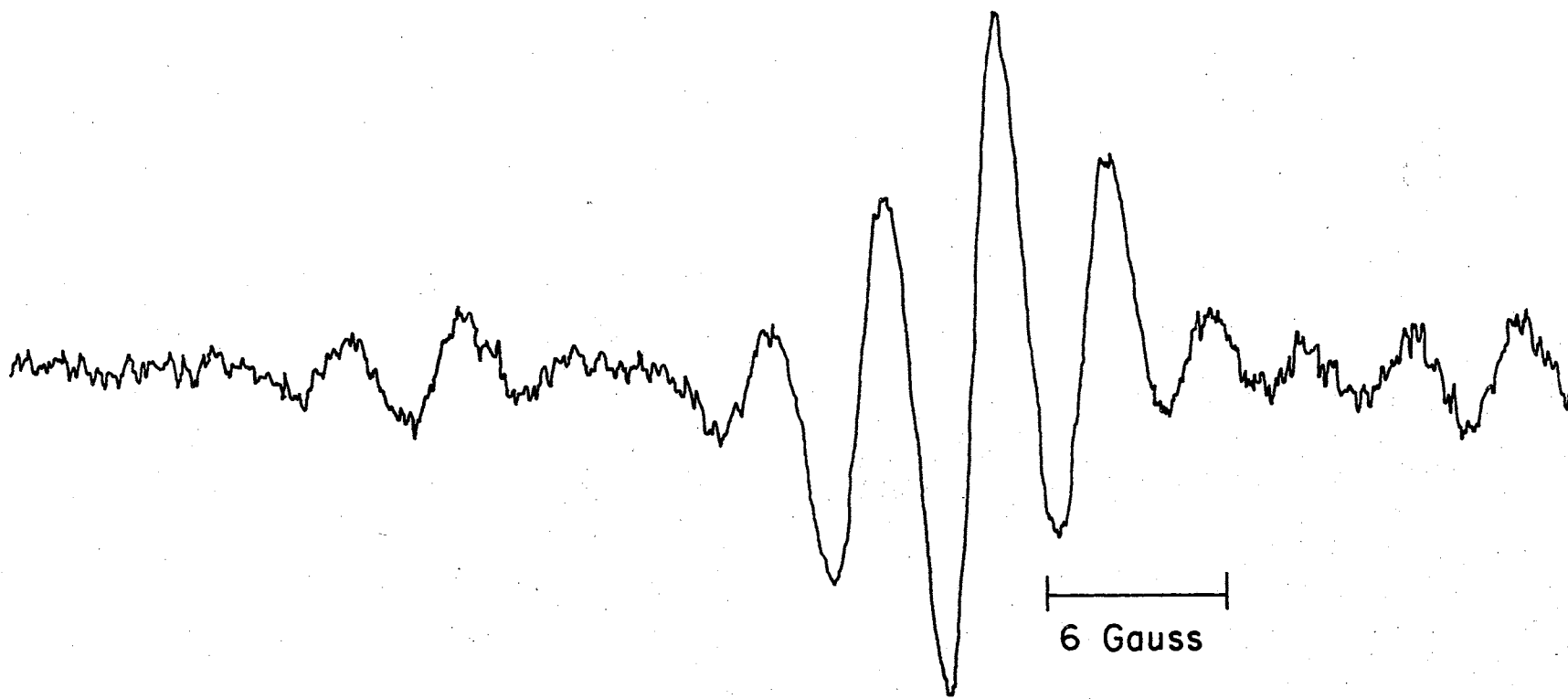


Figure 22. ESR Signal of Substitutional  $\text{Cr}^{3+}$  for  $H_0$  Parallel to the Y-axis.

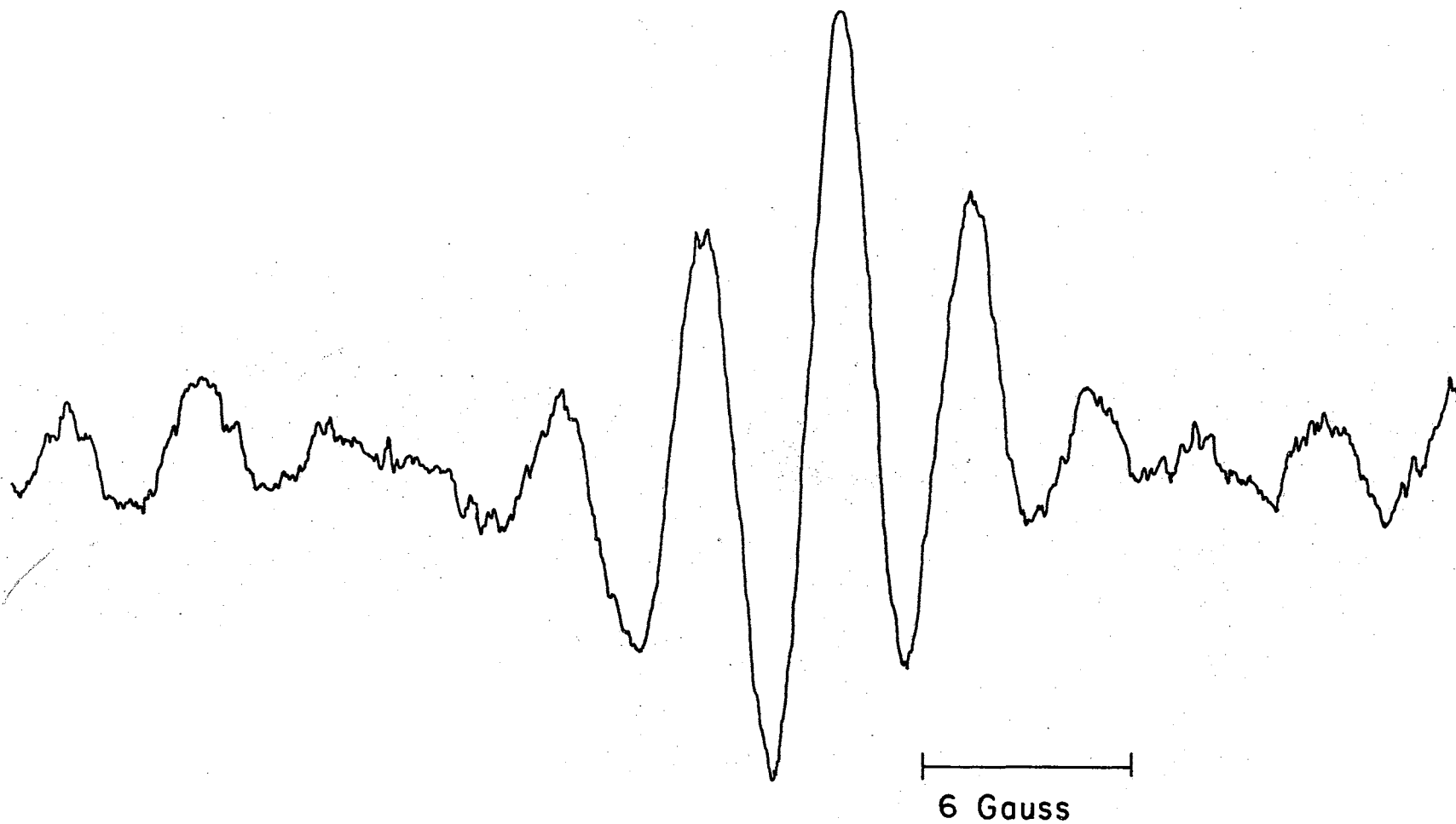


Figure 23. ESR Signal of Interstitial  $\text{Cr}^{3+}$  for  $H_0$  Parallel to the X-axis

to increase the number of centers by at least an order of magnitude seems called for if more work of this type is to be done on this ion.

On the other hand, particularly sensitive heat treatment dependence studies were made possible because of the small number of ions. These studies showed a very wide range of variation in signal amplitude and included the observations of Hou<sup>11</sup> as a small portion of the total treatment dependence. Further discussion of heat treatment effects will be deferred until the next chapter.

### ESR of $\text{Fe}^{3+}$ in $\text{SnO}_2$

Although substitutional  $\text{Fe}^{3+}$  in vapor-grown  $\text{SnO}_2$  has been reported previously,<sup>12</sup> two unreported effects were noted in flux-grown material. These consist of a heat treatment effect and the presence of a superhyperfine structure.

The ion identification, as in the case of  $\text{Ni}^{3+}$ , was facilitated through the use of crystals 137-K and 137-G supplied by Corning Glass. Crystals of this type were reported to contain 10-20 ppm iron impurity<sup>2</sup> which compares favorably with the determination of a number of spins corresponding to 10 ppm for the suspected  $\text{Fe}^{3+}$  impurity center (see Table VI). A signal observed by Hou<sup>11</sup> in vapor-grown crystals and attributed to the  $\pm \frac{3}{2}$  transition of  $\text{Fe}^{3+}$  agrees in line shape with that of the corresponding signal observed in this work. Also, as observed by Nakada et al.,<sup>12</sup> an orientation dependence of the suspected  $\text{Fe}^{3+}$  signal which is given in Figures 24 and 25 is very similar to that reported for substitutional  $\text{Fe}^{3+}$  in  $\text{TiO}_2$ .<sup>49</sup>

A distinct superhyperfine structure was observed for both the allowed  $\pm \frac{1}{2}$  and the forbidden  $\pm \frac{3}{2}$  transitions for certain orientations.

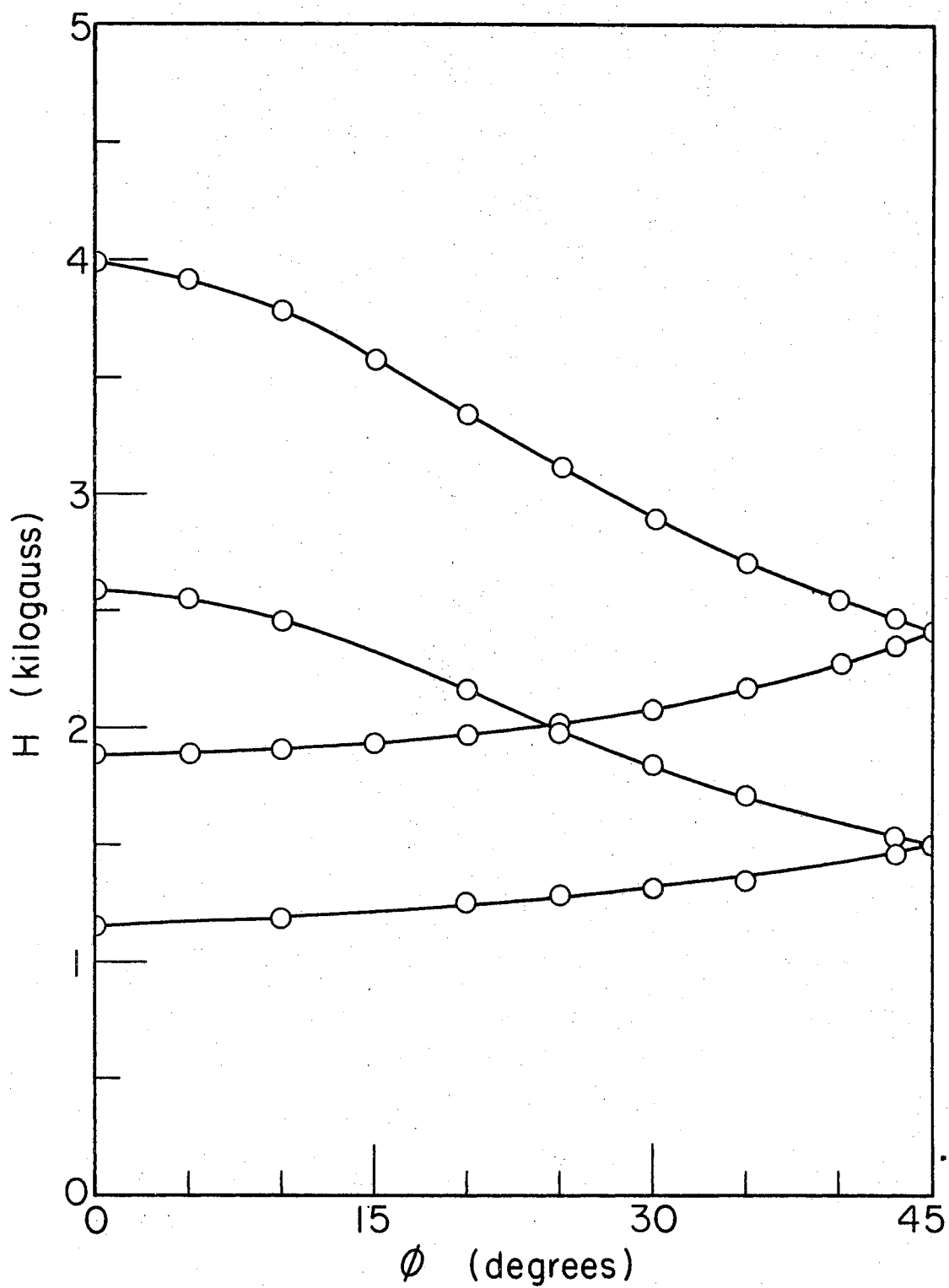


Figure 24. Orientation Dependence of  $\text{Fe}^{3+}$  ESR Signal in the  $\{001\}$  Plane

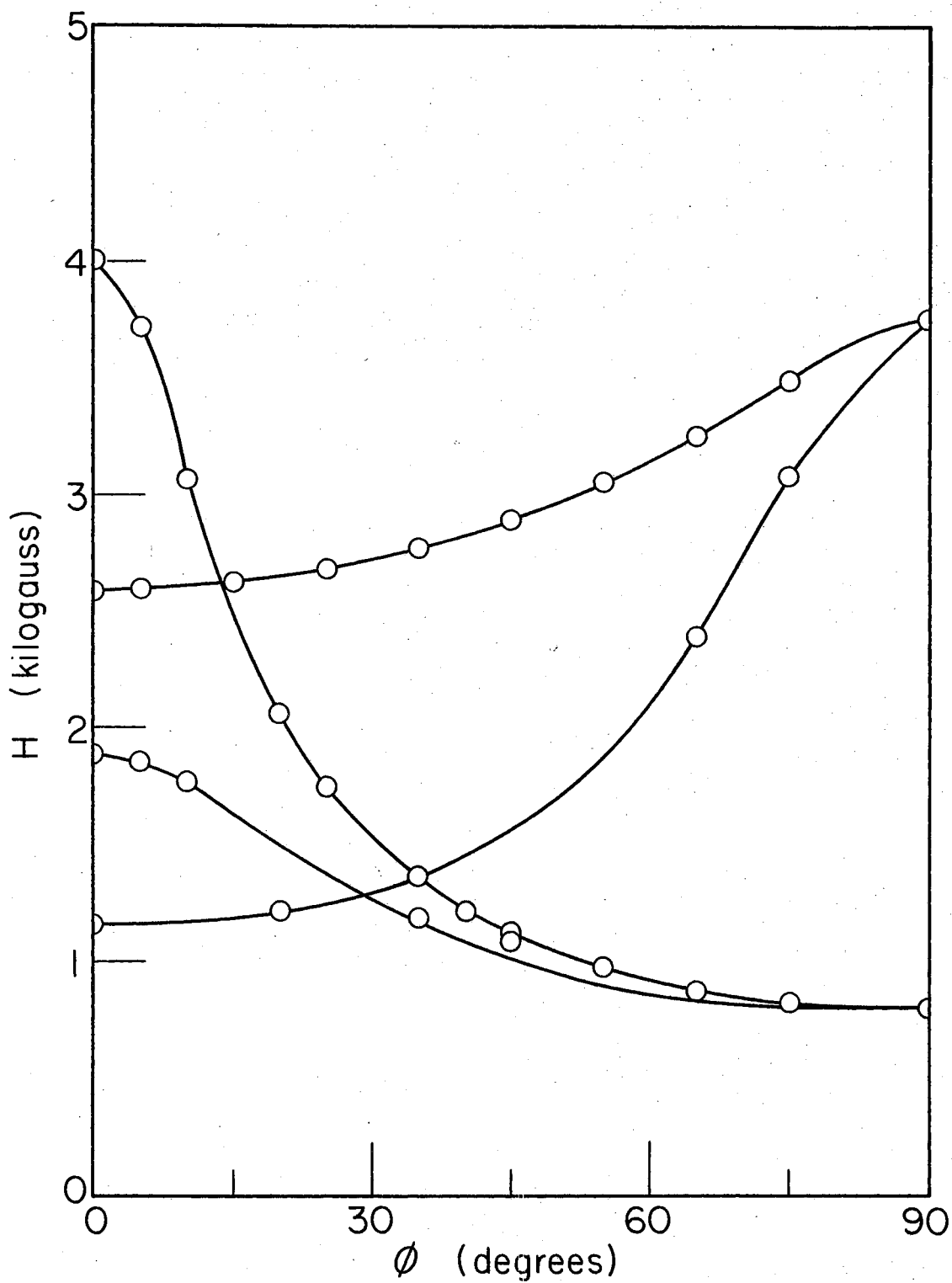


Figure 25. Orientation Dependence of  $\text{Fe}^{3+}$  ESR Signal in the  $\{110\}$  Plane

In the case of the  $\pm \frac{1}{2}$  transition, the superhyperfine structure collapsed when  $H_0$  was in the x-y plane (Figure 26), and became distinct when  $H_0$  was rotated out of this plane (Figure 27). However, for the  $\pm \frac{3}{2}$  transition the structure collapsed when  $H_0$  was parallel to the z axis (Figure 29) and emerged again when the magnetic field was rotated away from this direction.

The  $\pm \frac{1}{2}$  superhyperfine structure shown in Figure 27 is characteristic of that arising from the presence of two sets of inequivalent tins. The corresponding hyperfine constants are 5.1 gauss and 6.6 gauss. On the other hand, the  $\pm \frac{3}{2}$  structure shown in Figure 28 is characteristic of the presence of one set of equivalent tin ions and gives a hyperfine constant of 6.1 gauss.

An estimate of the number of tin ions in each set can be found by considering the percentage of tin nuclei having spin  $\frac{1}{2}$ . On this basis a theoretical intensity ratio shown in Table V has been given by Hou.<sup>11</sup>

TABLE V  
THEORETICAL INTENSITY RATIOS

$n/\sum m_I$	0	$\frac{1}{2}$	1	$\frac{3}{2}$	2
2	1	0.192	0.0094		
4	1	0.3606	0.0517	0.00335	0.00008
6	1	0.488	0.113		
8	1	0.599	0.186	0.033	0.0041
10	1	0.674	0.256		

For the  $\pm \frac{1}{2}$  transition the number of tin ions in each set are thus probably 6 and 2 since the ratios of the relative amplitudes are measured

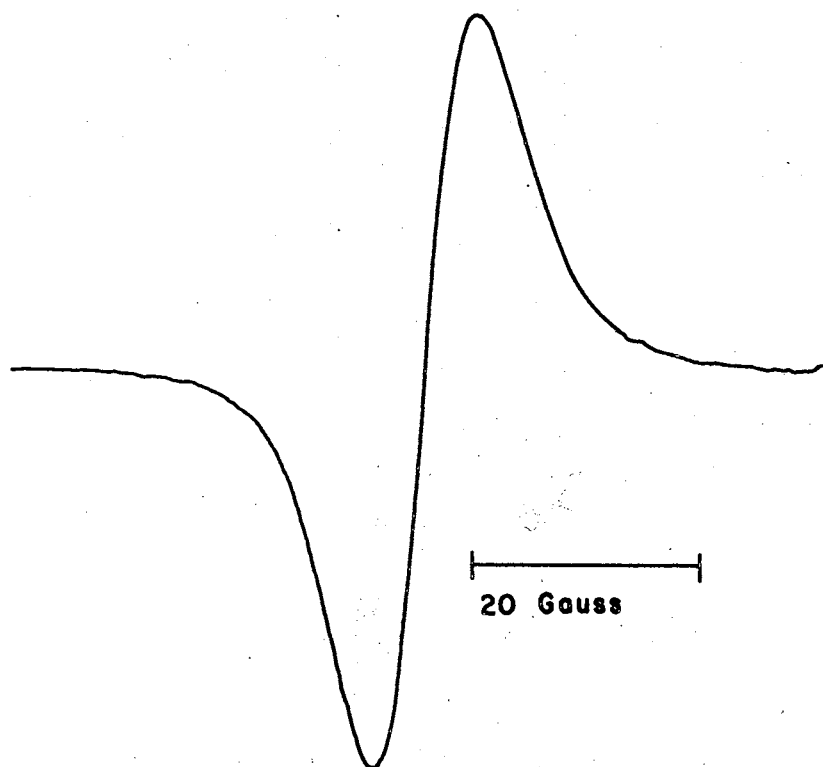


Figure 26. ESR Signal of  $\frac{1}{2}$  Transition of  $\text{Fe}^{3+}$  for  $H_0$  Parallel to the  $[110]$  Axis

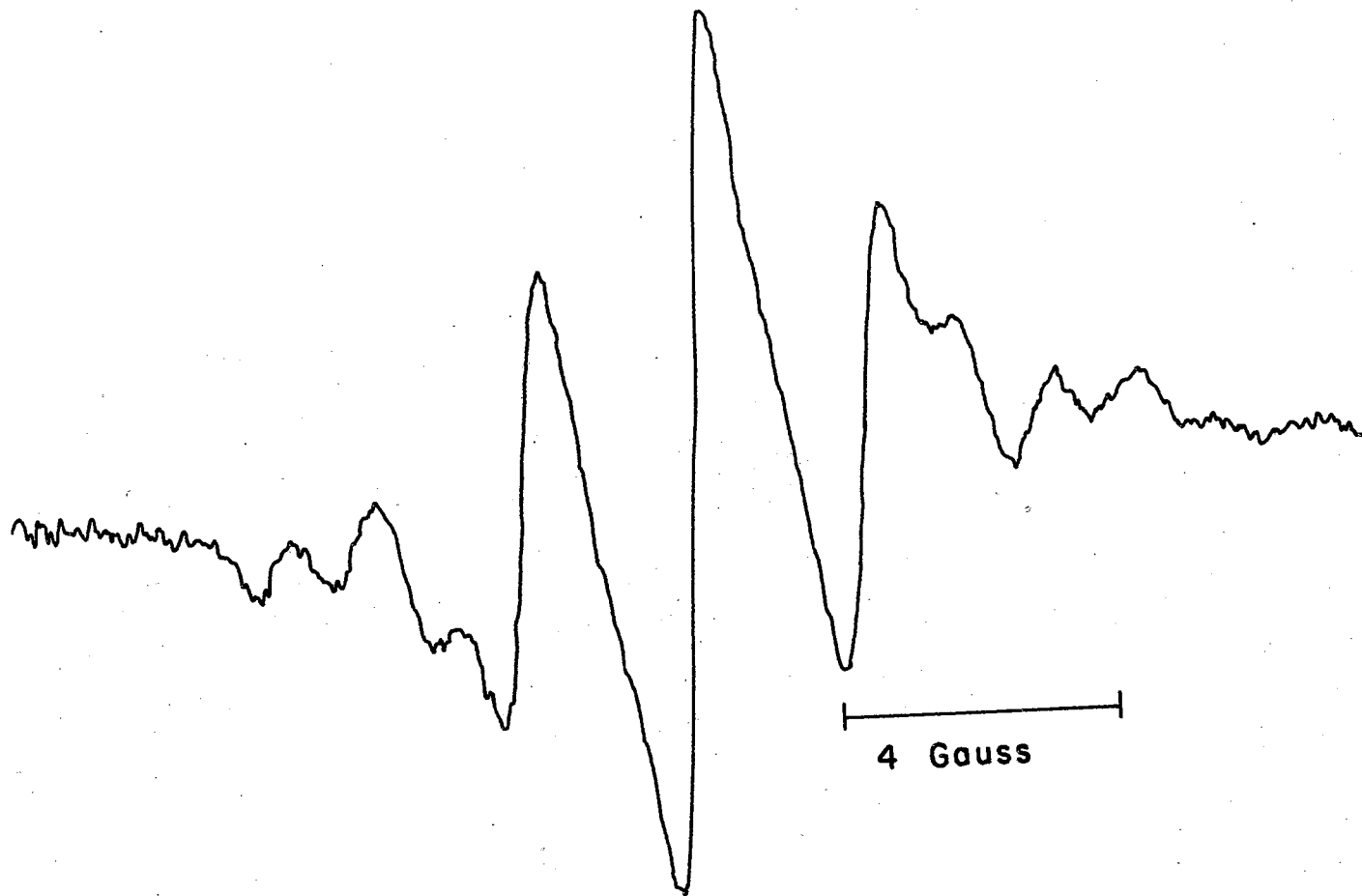


Figure 27. ESR Signal of  $\pm\frac{1}{2}$  Transition of  $\text{Fe}^{3+}$  for  $H_0$  Parallel to the [001] Axis



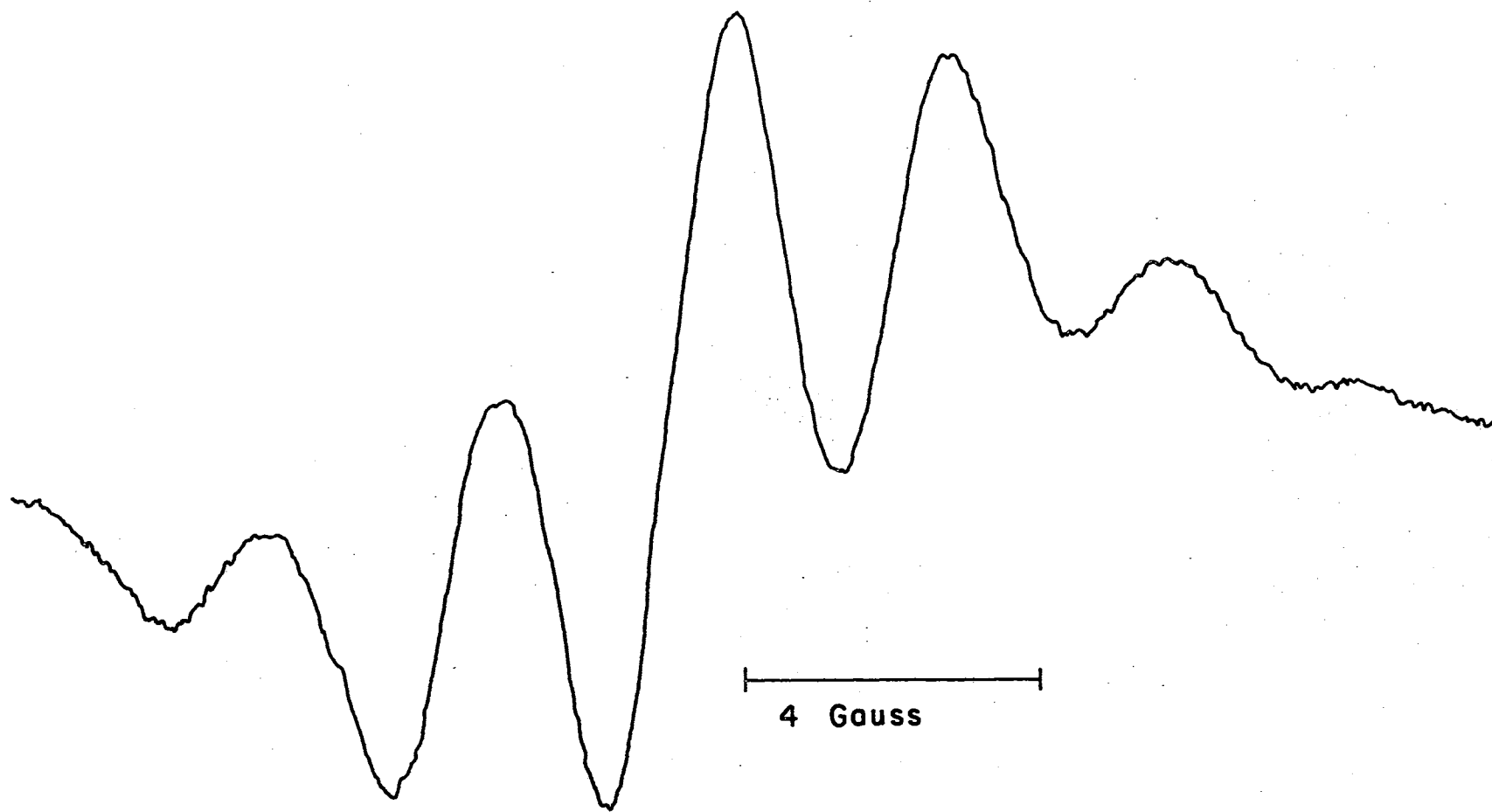


Figure 28. ESR Signal of the  $\pm \frac{3}{2}$  Transition of  $\text{Fe}^{3+}$  for  $H_0$  Parallel to the [110] Axis

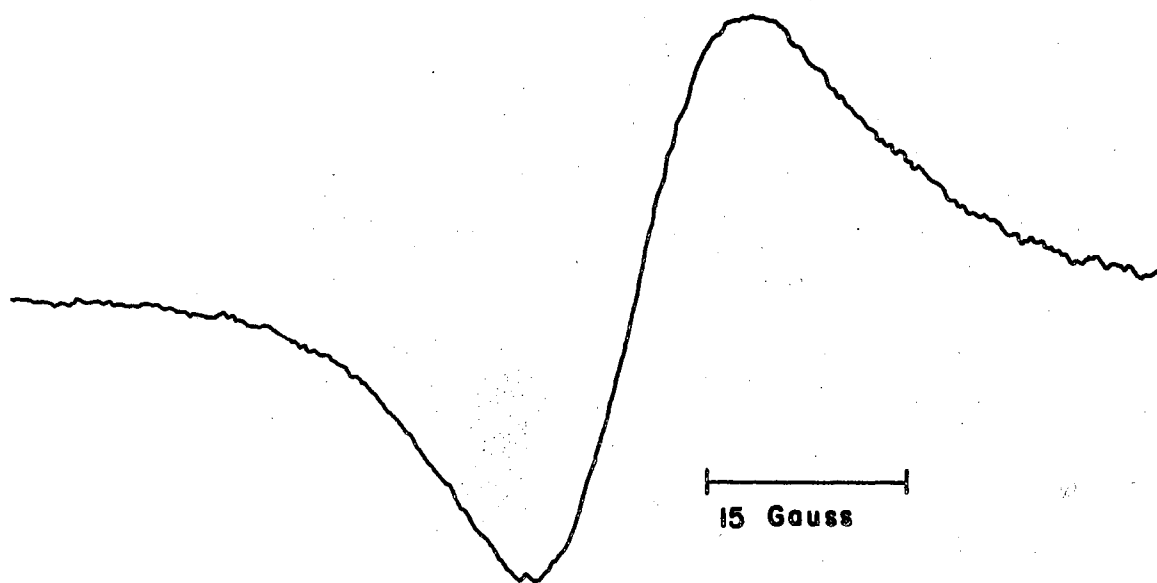


Figure 29. ESR Signal of the  $\pm \frac{3}{2}$  Transition of  $\text{Fe}^{3+}$  for  $H_0$  Parallel to the [001] Axis

to be about 0.52 and 0.174 respectively. These eight atoms become more equivalent for  $H_O$  parallel to the y axis since the intensity ratio is 0.58 for the  $\pm \frac{3}{2}$  signal shown in Figure 28.

A heat treatment dependence was also observed for this ion and will be discussed later.

#### ESR of an Unknown Interstitial Ion

A signal which appeared very weak for flux-grown  $SnO_2$  and which was rather large in  $SnO_2$  crystals grown by Corning Glass had an orientation dependence shown in Figure 30. From this preliminary data one can see that it probably comes from an interstitial ion in the distorted octahedral site. One infers this from the four inequivalent sites which collapse to two for  $H_O$  parallel to the  $[110]$  and  $[100]$  axes.

As can be seen from Figure 30, the magnetic axis of the center is aligned  $\approx \pm 5.5$  degrees from the  $[110]$  direction. This is considerably larger deviation than observed for the  $Cr^{3+}$  and  $Ni^{3+}$  interstitial ions. The most logical explanation of the signal is that it arises from a center which interacts much less strongly with the surrounding tin ions. This would allow the magnetic axis to take a direction more nearly coincident to the axis of the surrounding oxygen octahedron which is  $\pm 13^\circ$  from the  $[110]$  direction. Consistent also is the fact that no superhyperfine structure was observed as shown in Figure 31.

No identification of the ion can be made at this time. From the large orientation dependence of the resonances, however, one can conclude that it is a transition metal ion. One possibly is an interstitial  $Fe^{3+}$  ion. This possibility is suggested from the fact that the ratio of  $Fe^{3+}$  substitutional signal in the Corning crystals to that in

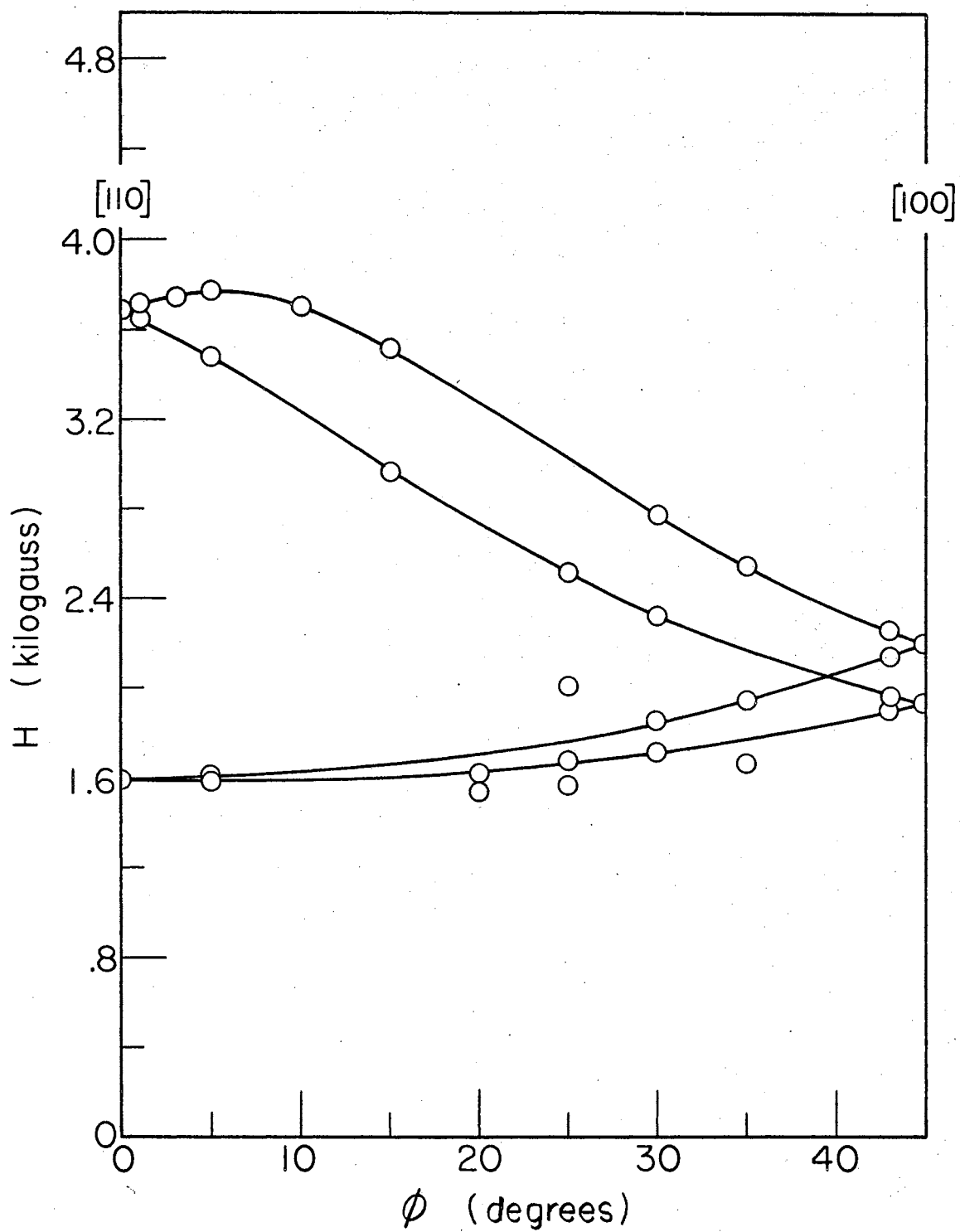


Figure 30. Resonance Due to Unknown Ions in the  $[001]$  Planes

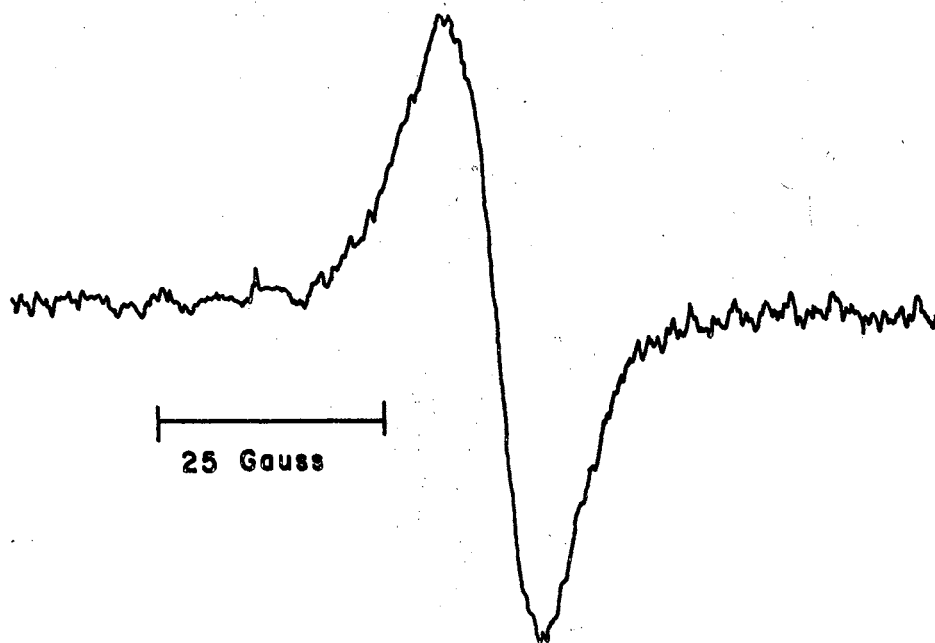


Figure 31. ESR Signal Due to Unknown Ion for  $H_0$  Parallel to the  $[110]$  Axis

flux-grown crystals is about the same as the corresponding ratio of the unknown signals. One might also expect a  $\text{Fe}^{3+}$  interstitial ion to exist in analogy with interstitial  $\text{Cr}^{3+}$  for charge compensation reasons. A possible way to check this hypothesis would be to diffuse iron into a flux-grown crystal in the same manner as was used in the present study of  $\text{Cr}^{3+}$  and  $\text{Ni}^{3+}$ .

#### Numbers of Observed Centers

The approximate number of each of the previously described paramagnetic centers present in a selected flux-grown sample (6-3) has been calculated and listed in Table VI. The assumption was made in these calculations that the number of centers is proportional to the area under the microwave absorption curve. Furthermore, the area under the absorption curves was taken to be proportional to the amplitude  $h_0$  and the square of the halfwidth of the derivative curve, i.e.,

$$N_0 = C_0 h_0 X_0^2$$

where  $N_0$  is the number of centers and  $C_0$  is a constant assumed to be the same for all ESR resonance lines observed in the study. Justification for this assumption lies in considering the integration of curves having Lorentz and Gaussian shapes as shown in Appendix I. It will be noted that areas under both of these curves--which are the most common shapes observed for ESR signals--follow the functional dependence of the above equation with the proportionality constants for the two cases differing by less than a factor of about five.

To allow the use of a larger calibrated sample, the further assumption was made that the signal amplitude is proportional to the amplitude

of the modulating field and to the gain settings. This should introduce only minor error in the range used.

TABLE VI  
SPIN CONCENTRATION IN TWO SELECTED SAMPLES

Sample	Ion	Total Spins ( $\times 10^{14}$ )	Spin Density ( $\times 10^{16}/\text{cm}^3$ )	Calculated (PPM) Ion Concentration
G-3	Ni <sup>3+</sup>	1.6	2.9	0.4
G-3	Cr <sup>3+</sup> (int.)	0.5	0.9	0.11
G-3	Cr <sup>3+</sup> (sub.)	0.2	0.4	0.05
G-3	Fe <sup>3+</sup>	0.3	0.55	0.07
A-137-K	Fe <sup>3+</sup>	67	72	10
A-137-K	Unknown	8.2	8.8	---
A-137-K	Ni <sup>3+</sup>	10	10.7	1.4

The previous equation then can be rewritten as

$$N_0 = C_0' \frac{h_0 X_0^2}{M G},$$

where M is the amplitude of the modulation field and G is the gain of the amplification circuit of the field modulation unit.

Using the above equation and a calibrated sample of dpph, a value is obtained for the system constant  $C_0'$ . The values shown in Table VI were calculated using this constant.

Numbers of individual centers as calculated in the above manner may be correct to no better than a factor of two or three, but this degree of uncertainty is not large when variations between individual crystals are considered.

## CHAPTER V

### RESULTS AND CONCLUSIONS CONCERNING HEAT TREATMENT EFFECTS

#### Preliminary Remarks

It has been noted previously that flux-grown  $\text{SnO}_2$  varies in color depending on its previous history of heat treatment.<sup>3</sup> Associated with the coloration, Eagleton<sup>50</sup> has found an optical absorption at 510  $\text{m}\mu$  for E1 c-axis. If a paramagnetic impurity were associated with this absorption center, one might expect a change in the ESR spectra to accompany the color change. With this in mind, a study was initiated to determine the nature of heat treatment effects on the ESR spectra.

The study was essentially divided into four parts. The first was merely an extension of the visual observations by Kunkle to determine which type of treatments might give the most significant results. The second consisted of observing the effect of these heat treatments on the various ESR spectra. The third was finding a model to explain the observed effect, and the fourth was making microbalance measurements to give support to the model.

#### Visual Observations

Observations were made of the color of the crystals after various heat treatments. The parameters varied were temperature of treatment, time of treatment, ambient gas, and rate of cooling. The general



results are as given below:

- (1) Treatments in air at a temperature range of 400-600°C always resulted in a pink crystal. The same treatment at 900°C followed by a rapid quench to room temperature resulted in a clear crystal. This same crystal when treated at 900°C and cooled slowly ( $\approx 2$  hours), again was pink.
- (2) In a nitrogen atmosphere the crystals always cleared after treatment at temperatures greater than 400°C. The necessary treatment time, however, varied from a few minutes at 900°C to a few weeks at lower temperatures near 400°C.
- (3) Reproducibility was very hard to achieve in vacuum heat treatments. Generally, the crystals cleared up at temperatures of  $\approx 500^\circ\text{C}$ , and became pink at temperatures of  $\approx 900^\circ\text{C}$  for a pressure in the range of  $10^{-2} - 10^{-3}$  torr. A treatment made by G. Baum at a pressure less than  $10^{-4}$  torr at a temperature of  $\approx 1000^\circ\text{C}$  resulted in a pink crystal. Quenching rates appeared unimportant.
- (4) Oxygen treatment always caused the crystals to become pink for temperatures greater than 400°C. The necessary treatment times were dependent on temperature in much the same fashion as the nitrogen treatments.
- (5) Helium treatments generally left the crystals unchanged at temperatures around 500°C and cleared them up at temperatures of about 900°C. Some doubt is involved in interpreting these results since impurities in the helium could easily be the dominant factor in the process.

(6) Only one treatment, at 350°C, was carried out in hydrogen.

The previously pink crystal became clear and a grayish film appeared on the surface of the crystal after eighteen hours.

It was suspected that this might contain excess tin.

Several qualitative conclusions were drawn from this study. Treatments in oxygen and nitrogen at different temperatures and times seemed to offer the greatest promise for a systematic study because of the reproducibility and the wide range of coloration observed. One might infer that results should be standardized by rapidly quenching the crystals to room temperature after each treatment. This is suggested by the treatments in air where the crystal, if cooled slowly, seemed to have the color characteristic of treatments at lower temperatures.

The above results indicate that the pinking process is not dependent only on the temperature or quenching rate. The nature of the ambient gas is of prime importance. In fact, one might hypothesize that the pink color is either directly or indirectly related to surface adsorption or bulk absorption of oxygen.

#### Heat Treatment Dependence of the ESR Spectra

A large heat treatment dependence of the ESR spectra has been noted for flux-grown  $\text{SnO}_2$  crystals. This heat treatment dependence includes that noted by Hou<sup>11</sup> as a small range of the total variations noted in the present study. Quantitative values, however, have not been obtained for this aspect of the work and only a qualitative description of the variations will be given.

The data upon which this description is based consist of the ESR spectra of flux-grown crystals in the highly reduced, highly oxidized,

and as-grown conditions. The oxidized condition was obtained by heat treating in an oxygen atmosphere at  $900^{\circ}\text{C}$  for twenty hours and then quenching to room temperature. The reduced condition was obtained with the same treatment using nitrogen instead of oxygen. It should be noted that the latter treatment resulted in such a low resistance that the spectrometer bridge could not be balanced. Thus the crystal was slightly reoxidized to a point where balance could be regained. Several spectra were also run for crystal conditions between these extremes and have the disadvantage that the treatment times were probably not long enough to insure a uniform oxidation condition throughout the crystal. This was suggested by subsequent weight loss measurements as shown in Figure 32 which indicated a time of about eighteen hours was needed to reach equilibrium at  $900^{\circ}\text{C}$ . Times for the intermediate condition treatments were usually a few minutes to a few hours.

The qualitative heat treatment dependence of the four identified signals is as given below:

(1) The  $\text{Cr}^{3+}$  interstitial ion signal has a maximum amplitude for the reduced condition, becomes quite small in the as-grown condition, and finally disappears in the oxidized condition.

(2) The  $\text{Cr}^{3+}$  substitutional ion signal is zero in the reduced condition, reaches a maximum when reduced slightly from the as-grown condition, and decreases to approximately three-fourths its maximum value for the oxidized condition.

(3) The  $\text{Fe}^{3+}$  ion gives rise to a signal of maximum amplitude when the crystal is in the oxidized state. This signal then becomes very small for the as-grown crystal and goes to zero for the reduced state.

(4) The ESR signal of  $\text{Ni}^{3+}$  remains constant except for the reduced

state where it is at about one-half amplitude. Some doubt exists as to whether this treatment effect is real since other losses associated with the low resistance tend to reduce the signal amplitude. However, it is felt at this time that the effect is real since such a large difference is hard to account for in the above manner.

It is noted here that the dependence of the  $\text{Cr}^{3+}$  signals reported by Hou, Summitt and Tucker<sup>11</sup> is consistent with the dependence seen in this study. The two points which they observed would correspond to a state slightly oxidized from the as-grown condition and reduced somewhat from the as-grown condition. The reason for the smaller range of signal change can be explained by the larger amounts of chromium and iron present in the crystals they investigated.

#### Proposed Model

The model previously proposed in the literature<sup>1</sup> to explain the heat treatment dependence of  $\text{Cr}^{3+}$  ion signals is found to be inadequate to explain the data of this study. Proposing that chromium substitutional ions jump to an interstitial position in the presence of a hydrogen ion cannot explain the changes observed for heat treatment in nitrogen. Furthermore no other signals are noted which could arise from iron and nickel ions changing site in the crystal.

A mechanism which will qualitatively explain both previously reported data and those of this study can be based upon the assumption that oxygen migrates in and out of the crystal during the treatment process causing an actual change in its stoichiometry. More specifically, oxygen leaves the crystal during the treatment in nitrogen or any other reducing atmosphere, releasing two electrons for each atom

involved. This raises the Fermi level and causes a change in the valence state of any impurity which has a ground state energy lying in this region. For example, if the Fermi level lies substantially below the  $\text{Cr}^{3+}$  interstitial ground state most of the interstitial chromium will be  $\text{Cr}^{4+}$ . Since  $\text{Cr}^{4+}$  is a  $d^2$  system containing an even number of electrons, one does not expect to observe a large ESR signal according to Kramers' theorem. However, as the Fermi level rises, more  $\text{Cr}^{3+}$  ions are present in the interstitial position and a signal is seen.

To help substantiate the proposed model a series of weight measurements were made in an effort to detect the loss of energy by the associated loss of weight. In these measurements a Mettler M5 microbalance with a sensitivity of  $\pm 2$  micrograms was used. The absolute accuracy is much less than this, however, since the samples were transferred in air from the treatment chamber to the balance pan, allowing the possibility that dust particles in the air might settle on the sample. The reliability of the data was thus inferred from the reproducibility of the data rather than from an a priori calculation.

The samples used in this experiment consisted of 1.2 grams of crystals whose individual size was on the order of  $1\text{mm} \times 1\text{mm} \times 1\text{mm}$ . These crystals were contained in a small quartz capsule and weighings were made of both the capsule and the crystals. The treatments were made in a Vycor tube connected to a small chamber allowing evacuation and the replacement of air with oxygen and nitrogen.

The quartz capsule was first weighed by itself after treatments in oxygen and nitrogen at  $750^\circ\text{C}$  for several hours. This resulted in no significant weight loss. A series of similar measurements with the samples in the capsule at this same temperature resulted in a reversible

weight change, with the weight gain in oxygen varying with the time of treatment. The maximum weight loss noted in a  $750^{\circ}\text{C}$  treatment was  $\sim 70$  micrograms.

A subsequent series of weight gains at  $900^{\circ}\text{C}$  in an oxygen atmosphere is shown in Figure 32 as a function of treatment time. The weight loss in nitrogen at this same temperature is shown in Figure 33. From this, one can see that reversible weight changes of about 74 micrograms take place which could correspond to losses and gains of oxygen.

The somewhat linear dependence of the weight loss vs. logarithm of time shown in the above figures is not what one would expect if the oxygen migration follows ordinary diffusion kinetics. To explore the possibility that rate limitation from this process is dependent on surface area, a series of similar weight measurements were made using sintered  $\text{SnO}_2$  samples<sup>51</sup>. These measurements gave inconclusive results. One of the problems involved here is that the effect of the much larger area and smaller crystalites of the sintered specimens may be to reduce the equilibrium times for treatment to something comparable with the quenching times.

On the basis of the proposed model and the heat treatment dependence of the ESR spectra a schematic diagram is given below for ordering the ion ground state energies in relation to the conduction band. Although no actual values can be assigned to these levels from this study alone, one can guess at some tentative values using other data. Since the  $\text{Cr}^{3+}$  substitutional signal vanishes only for the very highly reduced state, the  $\text{Cr}^{2+}$  substitutional ground state must be very close to the conduction band. From the large amounts of iron in the vapor-grown crystals one might suspect it to be the dominant factor in the

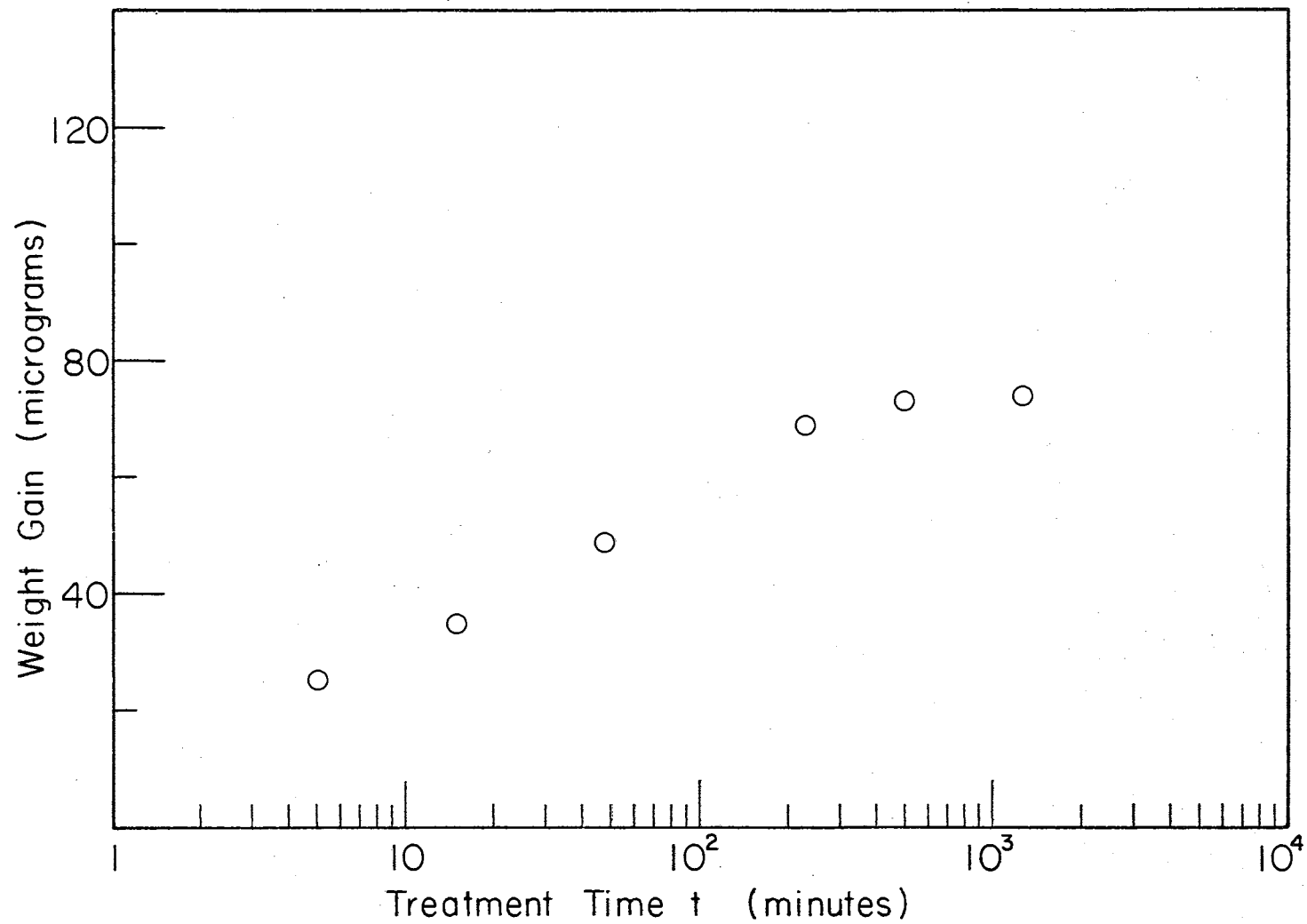


Figure 32. Weight Gain for Oxygen Heat Treatment

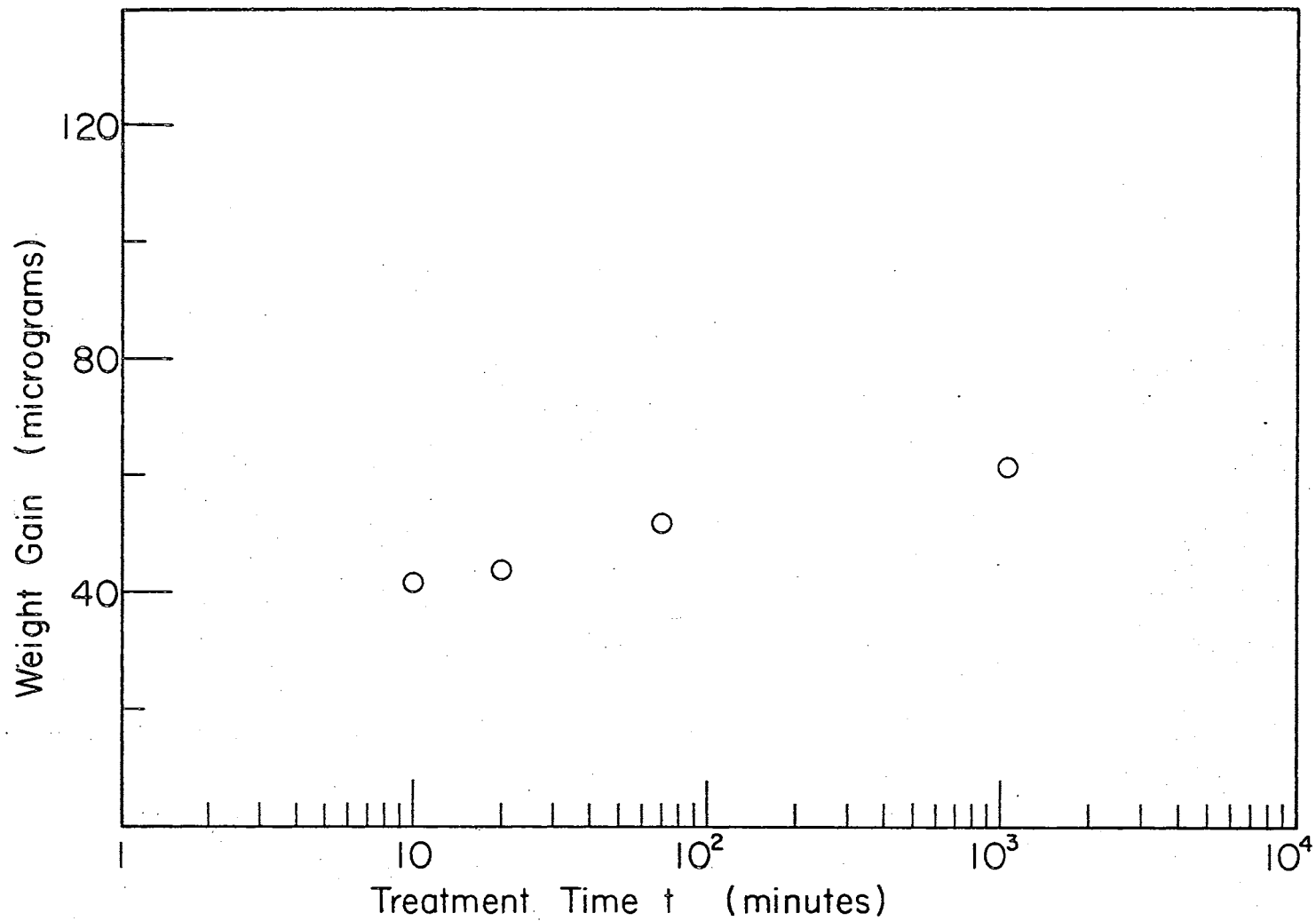


Figure 33. Weight Loss for Nitrogen Heat Treatment



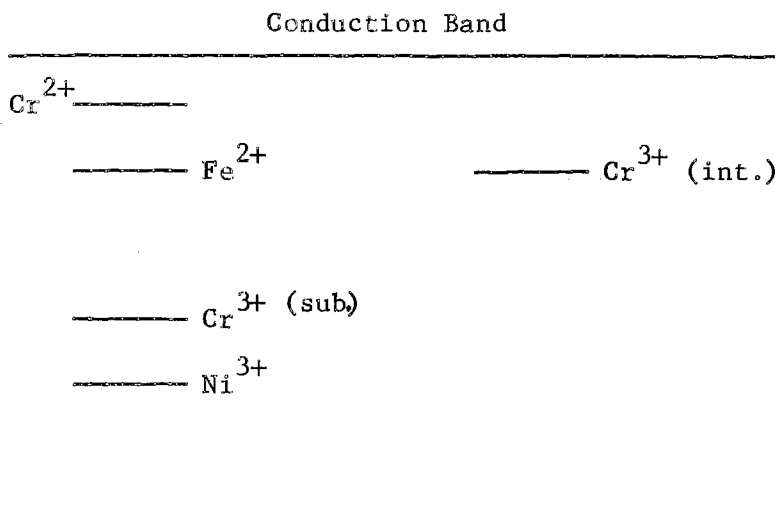


Figure 34. Ground State Energies

conductivity of the Corning Glass specimens. If this is the case, the  $\text{Fe}^{2+}$  ground state may be tentatively assigned an activation energy of 0.18 eV.<sup>7</sup> The  $\text{Cr}^{3+}$  interstitial ground state can be placed near the  $\text{Fe}^{2+}$  ground state because of the inverse behavior of  $\text{Cr}^{3+}$  and  $\text{Fe}^{3+}$  signals in the same treatment range. Since  $\text{Ni}^{3+}$  and substitutional  $\text{Cr}^{3+}$  signals decrease only for the very highly oxidized condition, their ground states have been placed lower in the forbidden gap, probably 1 eV or more below the conduction band. It should be emphasized again that the above diagram is presented to order the impurity ion states rather than to indicate possible activation energy values. Its value will lie in aiding future interpretation of experimental data obtained from electrical conductivity and photoelectronic analysis measurements.

## CHAPTER VI

### SUMMARY

In the course of this study the four most prominent ESR signals present in flux-grown  $\text{SnO}_2$  single crystals have been tentatively identified and the approximate number of centers counted. The analysis has been carried to the following extent for each of these:

- (1) Orientation data has been taken for  $\text{Ni}^{3+}$ , previously unreported in  $\text{SnO}_2$ , and has been interpreted on the basis of  $S = \frac{1}{2}$ ,  $g_x = 1.96$ ,  $g_y = 5.10$ , and  $g_z = 6.84$ . A superhyperfine structure of approximately 6 gauss has also been observed although detailed study awaits more heavily doped samples. A limited theoretical discussion of the g-values in terms of a distorted octahedral environment has also been made.
- (2) Preliminary data has been taken for both the allowed  $\pm \frac{1}{2}$  and forbidden  $\pm \frac{3}{2}$   $\text{Fe}^{3+}$  transitions. Since spin Hamiltonian parameters have been published previously,<sup>12</sup> no detailed study was made of these values. A superhyperfine structure, unreported in the above publication, was observed and received limited analysis. More detailed analysis of this signal is continuing.
- (3) The orientation dependence of  $\text{Cr}^{3+}$  interstitial and substitutional ions has been investigated. Since these resonances have been analyzed more extensively in the literature, the

main emphasis was identification of the ions and comparison with published results.

A heat treatment dependence was noted for all four resonances and studied. A model has been proposed to explain this dependence as well as the more limited dependence described previously for the two  $\text{Cr}^{3+}$  ions.<sup>11</sup> Further support for this model has been obtained through weight measurements. On the basis of this model a qualitative energy level scheme has been proposed for ordering the ground state energies in relation to the conduction band.

## CHAPTER VII

### SUGGESTIONS FOR FURTHER STUDY

It is suggested that there be an extension of the study of the  $\text{Ni}^{3+}$  ion. This would include three measurements. First, measurements should be made at liquid helium temperature, since there is a good chance the g-values measured in the present study contain contributions from the lower excited states. A crystal could be doped with nickel enriched in the isotope  $\text{Ni}^{61}$ . This would allow a measurement of the hyperfine structure for this isotope. If a crystal could be doped with about an order of magnitude more nickel than the crystals used in the present study, a more detailed investigation of the observed superhyperfine structure would also be possible.

In view of the very limited discussion of  $\text{Fe}^{3+}$  published to date, it would seem that a more complete analysis would be in order. This would include a computer analysis of the appropriate  $S = 5/2$  spin Hamiltonian to determine the parameters to a greater precision than that already published. An experimental and theoretical analysis of the superhyperfine structure would then be in order, in view of the rather strange behavior noted in the discussion (Chapter V). It should be mentioned here that orientation data--particularly at low fields--should be retaken in future study since the nuclear magnetic resonance probe operated unsatisfactorily at the low frequencies required.

A quantitative study of the heat treatment effects seems inviting

at this time. Since systematic data for establishing a model has been taken at only one temperature, it would seem that a series of micro-balance measurements at different temperatures would now be in order. Furthermore, similar measurements at different ratios of nitrogen to oxygen should be compared with measurements in vacuum to explain why heating in nitrogen seems to be more effective in reducing the samples than heating in vacuum. The linear relationship of weight change to logarithm of time also bears closer theoretical and experimental investigation to provide further insight into the specific mechanisms involved in the heat treatment process.

The model proposed in this work suggests an interesting new way of using ESR techniques in evaluating impurity ground state energies with respect to the  $\text{SnO}_2$  conduction band. This would be accomplished utilizing closely knit ESR and electrical conductivity measurements.

The procedure would be as follows: The crystal will be subjected to a series of heat treatments and an amplitude analysis will be made of an identified ESR signal to indicate the condition under which the Fermi level is lying at the ion ground state energy. Conductivity data as a function of temperature at room temperature and below will then be obtained to determine an activation energy equal to the energy difference between the ion ground state and the bottom of the conduction band. In this manner it seems at this time theoretically possible to determine activation energies for all of the heat treatment dependent signals present in the flux-grown crystals, together with any other ions with which  $\text{SnO}_2$  crystals could be doped to give heat treatment dependent signals.

In connection with the  $\text{Ni}^{3+}$  signal, it might also be informative

to analyze the spectra of  $\text{Co}^{2+}$  if it can exist in the  $\text{SnO}_2$  host. Since it has the same electronic configuration as  $\text{Ni}^{3+}$  the same form of spin Hamiltonian will be involved with the main difference arising from the charge. However, it probably would not be observed except at liquid helium temperatures. One would expect the  $\text{Co}^{2+}$  species to be found in a reduced state of the crystal, if it exists at all.

The ion which one would really expect to be present in the flux-grown crystals is the  $\text{Cu}^{2+}$  ion. Because of this it was originally felt that it was a likely origin of at least one of the observed signals. However, after reflection upon resonances of this ion in other materials, it now seems apparent that this was highly unlikely considering the conditions under which the experimental data were obtained. The  $\text{Cu}^{2+}$  ion is usually observed only at liquid helium temperatures, and even then only at low microwave powers because of its characteristic long relaxation time. If a resonance due to this ion could be found, however, it would offer an extremely good opportunity for both experimental and theoretical investigation because of its simple electronic  $d^9$  configuration.

A long range project which should be very worthwhile is a systematic study of rare earth ions in  $\text{SnO}_2$ . In addition to the basic knowledge to be gained from such an investigation, the possibility of a laser or maser application seems quite good. The maser application, however, might be prohibited by the large superhyperfine structure to be expected.

## BIBLIOGRAPHY

1. Kunkle, H. F. and E. E. Kohnke, *J. Appl. Phys.*, 36, 3961 (1965).
2. Marley, T. A. and T. C. Mac Avoy, *J. Appl. Phys.*, 32, 2504 (1961).
3. Kunkle, H. F., Unpublished Ph.D. dissertation, Oklahoma State University (1966).
4. Houston, J. E. and E. E. Kohnke, *J. Appl. Phys.*, 36, 3961 (1965).
5. Houston, J. E. and E. E. Kohnke, *J. Appl. Phys.*, 37, 3083 (1966).
6. Rutledge, J. L., Unpublished Ph.D. dissertation, Oklahoma State University (1967).
7. Marley, J. A. and R. C. Dockerty, *Phys. Rev.*, 140, A304 (1965).
8. Kohnke, E. E., *J. Phys. Chem. Solids*, 23, 1557 (1962).
9. Low, W. and E. L. Offenbacher, *Solid State Physics*, 17, 158 ff., Ed. F. Seitz and D. Turnbull, Academic Press Inc., New York (1965).
10. From, W. H., *Phys. Rev.*, 131, 961 (1963).
11. Hou, S. L., R. W. Summitt and R. F. Tucker, *Phys. Rev.*, 154, 258, (1967).
12. Nakada, R., E. Atsuko and T. Takahashi, *J. Phys. Soc. Japan*, 21, 188 (1966).
13. Pake, G. E., *Paramagnetic Resonance*, W. A. Benjamin, New York (1962).
14. Low, W., *Solid State Physics*, Supplement 2, Ed. F. Seitz and D. Turnbull, Academic Press Inc., New York (1960).
15. Slichter, C. P., *Principles of Magnetic Resonance*, Harper and Row, New York (1963).
16. Bleaney B., and K. W. H. Stevens, *Repts. on Prog. in Phys.* 16, 108 (1953).
17. Al'tshuler, S. A. and B. M. Kozyrev, *Electron Paramagnetic Resonance*, Academic Press, New York, (1964).

## BIBLIOGRAPHY (Continued)

18. Wigner, E., Nachr. Akad. Wiss. Gottingen Math-Physik. Kl. IIa, 546 (1932).
19. Kleiner, W. H., J. Chem. Phys., 20, 1784 (1953).
20. Tanabe, y., and S. Sugano, J. Phys. Soc. Japan, 11, 864 (1956).
21. Hamermesh, M., Group Theory, Addison-Wesley Publishing Company, Inc., Reading, Mass. (1962).
22. Ballhausen, C. J., Introduction to Ligand Field Theory, McGraw-Hill Book Company, Ind., New York (1962).
23. Cotton, F. A., Chemical Applications of Group Theory, Interscience Publishers, New York, (1963).
24. Tinkham, M., Group Theory and Quantum Mechanics, McGraw-Hill Book Company, Inc., New York (1964).
25. Wigner, E. P., Group Theory, Academic Press, New York (1969).
26. Bethe, H., Ann. Physik, 3, 133 (1929).
27. Rose, M. E., Elementary Theory of Angular Momentum, John Wiley and Sons, Inc., New York (1957).
28. Stevens, K. W. H., Proc. Phys. Soc., A65, 209 (1952).
29. Elliott, R. J. and K. W. H. Stevens, Proc. Roy. Soc. A218 553 (1953)
30. Judd, B. R., Proc. Roy. Soc. A227, 552, (1955).
31. Koster, G. F., J. O. Dimmock, R. G. Wheeler and H. Statz, Properties of the Thirty-Two Point Groups, M.I.T. Press, Cambridge, Massachusetts (1963).
32. Eyring, H., J. Walter, and G. Kimble, Quantum Chemistry, John Wiley and Sons, Inc., New York (1944).
33. Schiff, L. I., Quantum Mechanics 2d ed. P. 199, McGraw-Hill Book Company, Inc., New York (1955).
34. Bell, M. D., Unpublished Ph.D. dissertation, Oklahoma State University (1964).
35. King, J. P., Unpublished Ph.D. dissertation, Oklahoma State University (1966).
36. Wittke, J. P., J. Electrochem. Soc., 113, 193 (1966).



## BIBLIOGRAPHY (Continued)

37. Kikuchi, C., I. Chen, W. H. From and P. B. Dorsin, *J. Chem. Phys.*, 42, 181 (1965).
38. Yamaka, E. and R. G. Barnes, *Phys. Rev.*, 125 1568 (1962).
39. Low, W., *Phys. Rev.*, 109, 256 (1958).
40. Abragam, A. and M. H. L. Pryce, *Proc. Roy. Soc.*, A206, 173 (1951).
41. Tinkham, M., *Proc. Roy. Soc.*, A236, 549 (1956).
42. Gladney, H. M., *Phys. Rev.*, 146, 253 (1966).
43. Bleaney, B. and D. J. E. Ingram, *Proc. Roy. Soc.*, A208, 143 (1951).
44. Ingram, D. J. E. and J. E. Bennett, *J. Chem. Phys.*, 22, 1136 (1954).
45. Baker, J. M., W. Hayes, and D. A. Jones, *Proc. Phys. Soc.*, 73, 942 (1959).
46. Bose, A., S. Lahiry and U. S. Ghosh, *J. Chem. Phys. Solids*, 26 1747 (1965).
47. Sroubek, Z. and K. Zdansky, *J. Chem. Phys.*, 44, 7078 (1966).
48. Dunn, T. M., *Trans. Faraday Soc.* 57, 1441 (1961).
49. Carter, D. L. and Akira Okaya, *Phys. Rev.* 118, 1485 (1960).
50. Eagleton, R., Private Communication (1967).
51. Matthews, H. E., Unpublished Ph.D. dissertation, Oklahoma State University (1967).

## APPENDIX

### Integration of the Gaussian Curve

Consider a Gaussian curve of the form shown at the right and of analytical form,

$$f(x) = H \exp\left(-\frac{a^2 x^2}{2}\right). \quad (38)$$

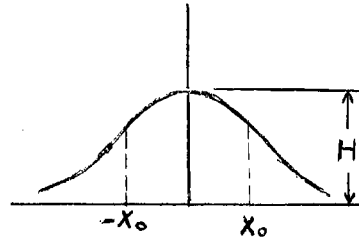


Figure 35. Gaussian Curve

Taking the derivative with respect to  $x$  gives an analytical expression,

$$\frac{\partial f}{\partial x} = -a^2 x H \exp\left(-\frac{a^2 x^2}{2}\right), \quad (39)$$

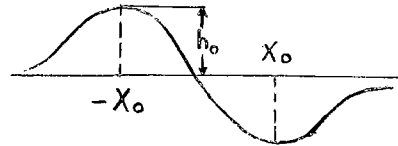


Figure 36. Derivative Curve

and a graphical form shown at the right. The distance  $2x_0$  is now the half width of the line.

Now taking the second derivative with respect to  $x$  one obtains

$$\frac{\partial^2 f}{\partial x^2} = -a^2 H \exp\left(-\frac{a^2 x^2}{2}\right) + a^4 x^2 H \exp\left(-\frac{a^2 x^2}{2}\right). \quad (40)$$

Setting  $\frac{\partial^2 f}{\partial x^2} = 0$  one has

$$-a^2 H \exp\left(\frac{-a^2 x^2}{2}\right) + a^4 x^2 H \exp\left(\frac{-a^2 x^2}{2}\right) = 0 \quad (41)$$

which reduces to

$$x^2 = \frac{1}{a^2} .$$

Since  $x_0$  shown in Figure 36 is the point where  $\frac{\partial^2 f}{\partial x^2} = 0$ , one now has  $x_0$  in terms of  $a$ , or

$$x_0^2 = \frac{1}{a^2} . \quad (42)$$

Substituting equation 42 into equation 39 one obtains

$$\left(\frac{\partial f}{\partial x}\right)_{x=x_0} = -\frac{1}{x_0} H \exp\left(-\frac{1}{2}\right) . \quad (43)$$

However  $\left(\frac{\partial f}{\partial x}\right)_{x=x_0} = -h_0$ , which after solving for  $H$  in equation 43 gives,

$$H = h_0 x_0 \exp\left(\frac{1}{2}\right) . \quad (44)$$

Substituting equations 44 and 42 into equation 38 yields

$$f(x) = + h_0 x_0 \exp\left(\frac{1}{2}\right) \exp\left(\frac{-x^2}{2x_0^2}\right) . \quad (45)$$

Integrating this we then have the area under Figure 35.

$$A = \int_{-\infty}^{\infty} f(x) dx = -h_0 x_0 \exp\left(\frac{1}{2}\right) \int_{-\infty}^{\infty} \exp\left(\frac{-x^2}{2x_0^2}\right) dx$$

$$A = \frac{\exp\left(\frac{1}{2}\right)}{\sqrt{2}} \pi h_0 x_0^2 . \quad (46)$$

Equation 46 thus gives the area under the Gaussian in terms of parameters measured from its derivative.

### Integration of the Lorentzian Curve

Consider a curve of Lorentzian form given by

$$f(x) = \frac{A}{x^2 + a^2} \quad (47)$$

Differentiating with respect to  $x$ , one obtains

$$\frac{\partial f}{\partial x} = \frac{-2Ax}{(x^2 + a^2)^2} \quad (48)$$

Again taking the derivative of equation 48 with respect to  $x$  and setting the result equal to zero gives,

$$\frac{\partial^2 f}{\partial x^2} = \frac{-(x^2 + a^2)^2 \cdot 2A + (2Ax) \cdot 2(2x) \cdot (x^2 + a^2)}{(x^2 + a^2)^4} = 0$$

or since the value of  $x$  when equation 48 is maximum value,  $x_0$  is  $(-x_0)$ ,

$$x_0^2 = \frac{a^2}{3} \quad (49)$$

Substitution of equation 49 into equation 48 then gives,

$$\left. \frac{\partial f}{\partial x} \right|_{x=x_0} = h_0 = \frac{2Ax}{(x_0^2 + 3x_0^2)^2} = \frac{A}{8x_0^3}$$

or

$$A = 8x_0^3 h_0 \quad (50)$$

Substitution equation 49 and 50 into equation 47 and integrating to find the total area under the curve,

$$\text{Area} = 8x_0^3 h_0 \int_{-\infty}^{\infty} \frac{dx}{x^2 + 3x_0^2} \quad \text{Area} = \frac{4\pi x_0^2 h_0}{3} \quad (51)$$

Thus the area of a Lorentzian curve in terms of parameters of the derivative curve is given by,

$$\text{Area} = Cx_0^2 h_0 \quad . \quad (52)$$

VITA

Jerald Arden Tunheim

Candidate for the Degree of

Doctor of Philosophy

Thesis: ELECTRON SPIN RESONANCE OF FLUX-GROWN STANNIC OXIDE SINGLE CRYSTALS

Major Field: Physics

Biographical:

Personal Data: Born in Marshall County, South Dakota, September 3, 1940, the son of Johannes and Annie Tunheim.

Education: Attended elementary school at Newport #3 district school, Marshall County, South Dakota; graduated from Langford High School, Langford, South Dakota, in 1958; received the Bachelor of Arts degree from South Dakota State University, Brookings, South Dakota, with a major in Engineering Physics, in June, 1962; received the Master of Science degree from South Dakota State University, with a major in Physics, in August, 1964.

Publications: "Alpha-Particle Models for  $\text{Si}^{28}$  and  $\text{S}^{32}$ ." Phys. Rev. 145, 722 (1966) with D. Nordstrom and G. Duffey; "Electron Spin Resonance of  $\text{Ni}^{3+}$  in Stannic Oxide. Bull. Am. Phys. Soc. 13, 71 (1968) with M. D. Bell, E. E. Kohnke, and W. J. Leivo.